

JOURNAL *of*  
UNDERGRADUATE  
REPORTS IN PHYSICS

VOLUME XXXI  
ISSUE 1

.....  
2022



JURRP

A PUBLICATION OF THE SOCIETY OF PHYSICS STUDENTS  
Available online at [www.spsnational.org](http://www.spsnational.org)

**Editor-in-Chief**

Brad R. Conrad

**Editor**

Will Slaton

**Managing Editor**

Kendra Redmond

**Art Director**

Aaron Hansen

**Layout Designer**

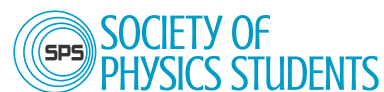
Hyun Joo Kim

**SPS President**

Kiril Streletzky,  
Cleveland State University

**SPS Director**

Brad R. Conrad



1 Physics Ellipse  
College Park, MD 20740-3841

301.209.3007 (tel)  
301.209.0839 (fax)  
sps@aip.org  
www.spsnational.org



Find SPS on:



**Journal of Undergraduate Reports in Physics**

(ISSN 0731-3764) is the publication of the Society of Physics Students, published annually by the American Institute of Physics. Printed in the USA. Standard postage paid at Freeport, OH. POSTMASTER: Send address changes to JURP, One Physics Ellipse, College Park, MD 20740-3841.

The American Institute of Physics is a federation of scientific societies in the physical sciences, representing scientists, engineers, educators, and students. AIP offers authoritative information, services, and expertise in physics education and student programs, science communication, government relations, career services, statistical research in physics employment and education, industrial outreach, and history of the physical sciences. AIP publishes *Physics Today*, the most closely followed magazine of the physical sciences community, and is also home to the Society of Physics Students and the Niels Bohr Library & Archives. AIP owns AIP Publishing LLC, a scholarly publisher in the physical and related sciences. [www.aip.org](http://www.aip.org)

**AIP Member Societies:**

- American Association of Physicists in Medicine
- American Association of Physics Teachers
- American Astronomical Society
- ACA The Structural Science Society
- American Meteorological Society
- American Physical Society
- Acoustical Society of America
- AVS: Science & Technology of Materials, Interfaces, and Processing
- Optica (Formerly The Optical Society)
- The Society of Rheology

**Other Member Organizations:**

- Sigma Pi Sigma physics and astronomy honor society
- Society of Physics Students

# Table of Contents

2022 • VOLUME XXXI, ISSUE 1

**LETTER FROM THE EDITORS** ..... 1

The Rotation Curve of the Milky Way Galaxy as Evidence for Dark Matter ..... 2

A Simple Model for Understanding Cloud Diffusion on a Brown Dwarf ..... 7

An Introduction to Quantum Computing..... 11

On the Resonances of Coupled Qubit–Cavity Systems..... 14

Using  $\gamma\gamma$ -Coincidence Spectroscopy to Identify Natural Radiation in Soils Near the Mississippi River ..... 20

Development of an Optical Tweezers Demonstration ..... 26

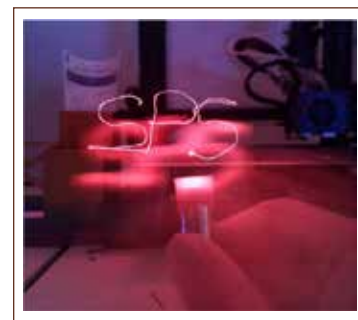
Dielectric Properties of Nanostructured ZnO Using Impedance Spectroscopy ..... 30

Remarkable Topological Features of Electronic Band Dispersion of IrGa and RhGa Compounds from First Principles..... 33

Preparing a Manuscript for Publication..... 41



21



29

# Letter from the Editors

by Brad R. Conrad, Director, SPS and Sigma Pi Sigma; Will Slaton, Professor and Coordinator of Engineering Physics, University of Central Arkansas; and Kendra Redmond, Editor, *The SPS Observer*



ABOVE: Brad R. Conrad,  
Photo courtesy of SPS National Office.



“The mere formulation of a problem is often far more essential than its solution, which may be merely a matter of mathematical or experimental skill. To raise new questions, new possibilities, to regard old problems from a new angle requires creative imagination and marks real advances in science.”

—Albert Einstein

The Society of Physics Students, which is supported by the American Institute of Physics (AIP), is proud to produce the *Journal of Undergraduate Reports in Physics* (JURP). JURP launched in 1981 out of Guildford College, then called the *Journal of Undergraduate Research in Physics*, as a publication dedicated to sharing the research pursuits of undergraduates in **physics, astronomy, and related fields**. JURP’s founder, Dr. Rexford Adelberger, described its origins in Volume 10:

The research projects that most undergraduate students can complete during their brief stay at college seldom met the rigorous requirements of [professional journals]. This does not mean that the work lacked new physics and clever insights, it was just not of the scope expected of people whose profession is to do research in physics. Yet, we were convinced that the learning and rewards that come from writing up the research in a professional manner and learning to communicate using the professional media had a definite place in the undergraduate program of study in physics.

Undergraduate research and scholarship are the bedrock of physics and astronomy education and indispensable tools for deep learning. As Einstein alluded to in his statement above, physics is not necessarily about reaching a solution or a final value but the process of exploring the problem itself. Sharing that exploration is an essential part of being a scientist. We must learn from each other to advance. JURP provides an outlet for undergraduates to participate in this vital process.

There is no cost to publish in JURP beyond an SPS membership. All papers are peer reviewed by experts, and published papers are given a DOI by AIP Publishing. Print copies of JURP are sent to all SPS members each summer, and the articles are also published and archived online. As you reflect on your summer research experience or begin a new project in the coming year, keep JURP in mind. We would love to share your work in the 2023 issue. You can learn more about the JURP submission process at [www.spsnational.org/jurp](http://www.spsnational.org/jurp).

Communicating research is an integral component of scientific inquiry and a linchpin of the discipline. We hope you enjoy this issue, learn from your colleagues, and are inspired to contribute if you so desire. There is so much fun to be had! //

*JURP is no small effort and takes a team of writers, reviewers, and editors to realize. SPS National would like to extend a special word of appreciation to Dr. Will Slaton of the University of Central Arkansas for his steadfast commitment to the journal and willingness to review and provide meaningful feedback on all submissions. We would also like to thank our reviewers for providing invaluable support and feedback to JURP authors.*

# The Rotation Curve of the Milky Way Galaxy as Evidence for Dark Matter

Huma Jafree,<sup>a)</sup> Rebekah Polen,<sup>b)</sup> Deonna Woolard, and Rachele Dominguez

Randolph-Macon College, 304 Henry Street, Ashland, Virginia, USA

<sup>a)</sup>Corresponding author: humajafree@go.rmc.edu

<sup>b)</sup>Corresponding author: bekahpolen@go.rmc.edu

**Abstract.** We present neutral hydrogen observations of the plane of the Milky Way galaxy between  $0^\circ < l < 80^\circ$  galactic longitude on the 20-meter telescope at the Green Bank Observatory. These radio spectroscopic signatures returned the 21-cm line of neutral hydrogen at various offsets due to the Doppler shift. By calculating orbital speeds relative to the galactic center, velocity was plotted against radial distance to map the rotation curve of the Milky Way galaxy. The distribution of luminous matter suggests that orbital velocity should fall off at large distances, but empirical observations show otherwise. An abundance of mass which cannot be detected is responsible for this phenomenon, known as dark matter. Although its nature is not understood, dark matter is easily observed indirectly by galactic rotation curves. Our observations confirm that the velocity of the Milky Way's disk is fairly constant even at large distances from the center of our galaxy, Sagittarius A\*.

## INTRODUCTION

In 1933, Swiss astronomer Fritz Zwicky found surprising results when taking radial velocity measurements of galaxies in the Coma cluster [1]. Using the virial theorem for the first time in astronomy, he estimated the mass of the galaxy cluster and found its corresponding velocities. At far distances from the galaxy cluster's center he found that the velocity dispersions were much larger than expected, suggesting that the cluster's density was higher than the one calculated from observable luminous matter [2]. The presence of this seemingly invisible matter in abundance around the edges of galaxies was named dark matter [2]. Evidence for dark matter increased over the next few decades. One of the most prominent studies to confirm its presence was conducted by Vera Rubin et al. [3], mapping galactic rotation curves of spiral galaxies. Neutral hydrogen (HI) emissions are easily detectable over the entire radial extent of spiral galaxies, and this is the most commonly used method while measuring rotation curves [4].

There are two major methods of indirect detection of dark matter; Zwicky's method, using velocity dispersions in galactic clusters, and Rubin's method, measuring velocity as a function of radius in individual galaxies. Currently, dark matter's composition remains largely unknown. Massive compact halo objects (MaCHOs) are unassociated baryonic celestial objects that emit little to no radiation [5]. MaCHOs, although contributing to the dark/luminous matter ratio, only comprise a tiny fraction of dark matter as a whole [6].

Weakly interacting massive particles (WIMPs) are the current leading candidate for dark matter but have never been detected. Particle observation and research regarding WIMPs remains a fundamental goal in astrophysics and the field of cosmology today [5]. There are several other models for dark matter particles such as axions, Higgs doublets, sterile neutrinos, and supersymmetric particles among other candidates that are active areas of research in direct detection [7].

This research aims to confirm known results of the rotation curve of the Milky Way galaxy using neutral hydrogen emissions along the galactic plane to reveal that velocity does not have a Keplerian falloff like  $r^{-1/2}$ . Instead, velocity tends to flat-line like  $r^0$ . Using classical mechanics, this inconsistency is revealed, which suggests the presence of a large amount of dark matter compared to normal luminous matter. The relationship between apparent luminosity of matter,  $L$ , and its mass,  $M$ , is given by the mass-luminosity relation [6]:

$$L \propto M^{3.5}. \quad (1)$$

Simply put, dark matter's existence is derived from the observation that material in the Milky Way is moving too fast. Mass is the only factor, according to classical mechanics, that can increase orbital velocity in this manner. To show this, only classical equations are necessary with the assumption of spherical mass distribution of luminous matter. Equation (2) is Newton's universal law of gravitation set equal to Newton's second law where acceleration is represented as angular acceleration. Here,  $G$  is the gravitational constant  $6.67 \times 10^{-11} \text{ m}^3 \text{ kg}^{-1} \text{ s}^{-2}$ ,  $r$  is radius from the galactic center,  $M$  is enclosed mass within the radius  $r$ ,  $v$  is orbital velocity, and  $m$  is an arbitrary mass at radius  $r$ .

$$G \frac{Mm}{r^2} = \frac{mv^2}{r} \quad (2)$$

Equation (2) can be algebraically simplified to give the orbital velocity in Eq. (3).

$$v = \sqrt{\frac{GM}{r}} \quad (3)$$

If Eq. (3) is rearranged, it is easier to see how mass affects the change in velocity with respect to  $r$ . Since  $G$  is a constant, the only variable in the equation affecting the observed result  $v$  is the mass. Here, Eq. (4) shows how  $v$  falls off like  $r^{-1/2}$ , the definition of a Keplerian falloff.

$$G^{-1/2}v = M^{1/2}r^{-1/2} \quad (4)$$

The Milky Way galaxy is more complicated than a spherical model suggests in that it is shaped like a disk and is not cylindrically symmetrical. However, more sophisticated models taking this geometry into account still predict a Keplerian falloff [8].

Velocity empirically does not fall off like  $r^{-1/2}$ ; rather, previous studies, including Fig. 1, indicate that velocity levels off to  $r^0$  [6,9,10,11,12]. Therefore, for velocity to be higher, mass must be greater than what we can estimate with luminous matter.

## METHODS AND OBSERVATIONS

### Specifications of the 20-Meter

In order to map the rotation curve of the Milky Way galaxy, observations were taken on the 20-meter telescope every 5-10° declination along the galactic plane beginning at -30°, the location of Sagittarius A\*. These coordinates were converted to galactic longitude  $l$  and translated to observations taken between  $0^\circ < l < 80^\circ$ . The telescope was configured to take "on/off" observations of each set of coordinates for a duration of 60 seconds and an integration time of 1 second. Off observations were taken -5° right ascension ( $\alpha$ ) and -5° declination ( $\delta$ ) from the target observation. On/off observations show a difference in the amount of detected neutral hydrogen on the galactic plane compared to neutral hydrogen off the galactic plane. Since the galactic plane is very rich in hydrogen and dense with stars and material, there is a very strong neutral hydrogen detection on the plane which can be reliably used to calculate velocity at radial increments from the galactic center. We checked that the on observations were correctly aligned on the plane of the galaxy by visually confirming that the off observations were only noise. Optical problems such as extinction do not affect this data, since these observations are taken in the radio frequency. In radio frequencies, we can see all of the hydrogen in the entire line of sight to the other end of the galaxy.

Our observations were taken on high-resolution mode, which has a bandwidth of 15.625 MHz and 1024 channels. The frequency associated with neutral hydrogen is 1420.41 MHz, also known as the 21-centimeter line. For observing neutral hydrogen, we used a center frequency of 1420 MHz and a secondary frequency of 1480 MHz, meaning that the range of the collected data was 1420-1480 MHz. These parameters were chosen to ensure a clear measurement of the 21-cm line while avoiding public radio frequency interference (RFI) that would compromise the data. The 20-meter telescope is connected to the SkyNet Robotic Telescope Network through the University of North Carolina Chapel Hill to be operated remotely. SkyNet does not produce FITS files for on/off observations that yield spectral line results; rather, SkyNet has its own user interface which cannot be exported. Peak frequencies from our observations could be ascertained within 0.005 MHz on the interface and recorded for mathematical manipulation within Mathematica and JupyterLab, using Python [13-15].

## Calculating Velocity from the Peak Frequency

Neutral hydrogen emits an electromagnetic wave resulting from a transition between a hyper-fine splitting of the ground state. This detected emission line is commonly referred to as the 21-centimeter line and corresponds to a classically forbidden spin flip transition of neutral hydrogen [16].

Observed peak frequencies of neutral hydrogen, however, are offset from the known frequency due to its velocity relative to Earth. Therefore, a speed can be calculated using the Doppler shift equation, Eq. (5), and the difference in observed frequency and known frequency, where  $v_{rel}$  is the velocity relative to the observer in  $\text{km s}^{-1}$ ,  $c$  is the speed of light at  $3 \times 10^5 \text{ km s}^{-1}$ , and  $f_{obs}$  is the peak frequency from the observation in MHz [6]:

$$v_{rel} = c \left( \frac{1420.41 \text{ MHz} - f_{obs}}{1420.41 \text{ MHz}} \right). \quad (5)$$

The Doppler shift equation yields the velocity of the gas relative to the observer, but not an orbital velocity relative to the galactic center. To calculate the orbital velocity relative to the galactic center,  $v_{orb}$ , we used the tangent point method (TPM) [17]. The TPM, Eq. (6), relies on the assumption that the extremum of an HI observation is tangent to the galactic center.  $V_{LSR}$  is a constant called the local standard of rest, which is the average velocity of material at the solar circle  $R_{solar}$ .  $R_{solar}$  is the distance of our sun from the galactic center. We take  $V_{LSR}$  to be  $220 \text{ km s}^{-1}$  and  $R_{solar}$  to be 8 kpc according to Sofue et al. [17,18]. Here,  $l$  is the galactic longitude of the measurement and  $R$  is the radius of the measurement from the galactic center in kpc.

$$v_{rel} = R_{solar} \sin(l) \left( \frac{v_{orb}}{R} - \frac{V_{LSR}}{R_{solar}} \right) \quad (6)$$

Using the  $v_{rel}$  values calculated from Eq. (5), we rearrange Eq. (6) to find values for both the distance from the galactic center and the orbital velocity for every observation. Algebraic manipulation of Eq. (6) yields both of these equations, Eq. (7) and Eq. (8).

$$R = R_{solar} \sin(l) \quad (7)$$

$$v_{orb} = v_{rel} + V_{LSR} \sin(l) \quad (8)$$

These equations provide the necessary information to plot the velocity  $v_{orb}$  as a function of radius  $R$ .

## RESULTS

A total of 13 observations were taken between  $0^\circ < l < 80^\circ$ . Passing the maximum frequencies through Eqs. (5)-(8), a distance and orbital velocity relative to the galactic center is obtained for each observation and represented in Fig. 1. Collected data is overlaid with the curve fit parameters of an array of rotation curve samples from more comprehensive papers. This figure suggests that the results of this study are in close agreement with several different surveys containing data from over a thousand galaxies at distances  $R > 4 \text{ kpc}$  [19].

For distances  $R < 4 \text{ kpc}$ , the collected data points are below the model curves. This deviation may be due to the TPM itself, since this method is considered difficult to use at distances very close to the galactic center and beyond  $90^\circ$  galactic longitude. The tangent point method can present several potential problems in calculating orbital velocities relative to the galactic center. The TPM relies on the assumption that the extremum of the HI measurement is tangent to the galactic center. However, at distances less than 4 kpc the bar of the Milky Way galaxy can produce highly noncircular orbits [20]. The HI measurements are often broadened by turbulence, which can affect the observed peak frequency. Additionally, the highest velocity gas is not necessarily directly on the galactic plane at a galactic latitude of  $b = 0^\circ$  [21].

The deviation, however, may be a real feature of the Milky Way galaxy. The TPM is a valid method of calculating velocity close to Sagittarius A\* [17]. Reid et al. makes a similar observation of low velocity values in the  $0 < R < 4 \text{ kpc}$  range in Fig. 11 of [20] using trigonometric parallaxes and proper motions.

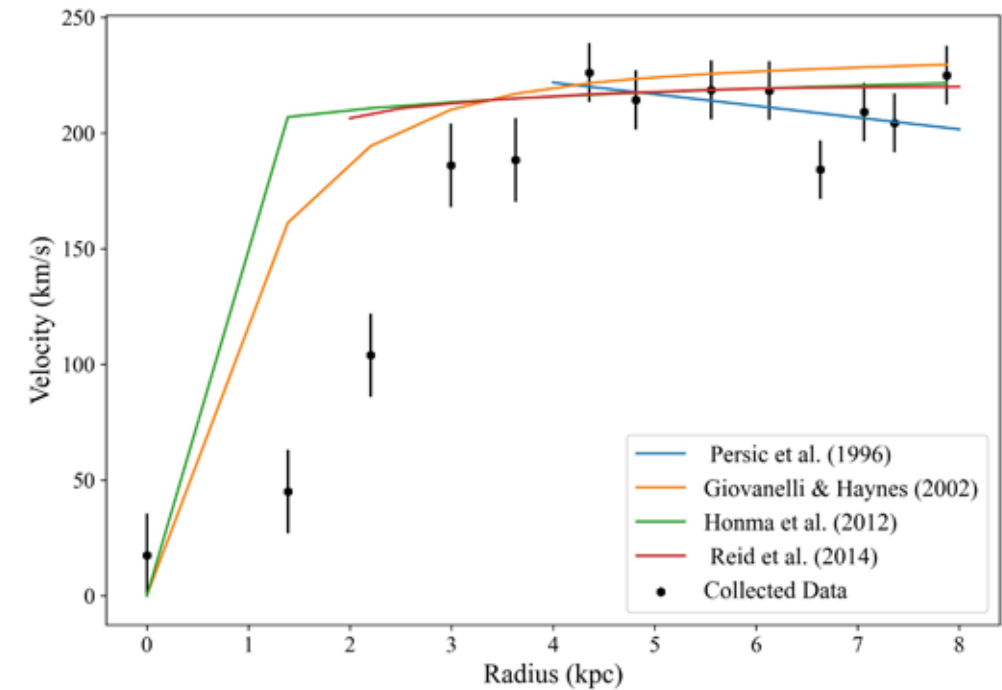


**FIGURE 1.** Velocity, as calculated using Eq. (8), is plotted against distance from the galactic center at  $l = 0^\circ$  to  $l = 80^\circ$ . These data points show a stabilization in velocity near  $200\text{-}220 \text{ km s}^{-1}$ . Collected data is compared with several expressions for the rotation curve by Persic et al. [12], Giovanelli and Haynes [9], Honma et al. [11], and Reid et al. [10]. Error bars represent random error as described in the text.

Velocity appears to stabilize at around  $220 \text{ km s}^{-1}$ , which is similar to the LSR. In order to estimate the random error in our data, we calculated the average distance between a line of best fit and the collected points. For points  $R < 4 \text{ kpc}$ , we assume a linear curve, and for points  $R > 4 \text{ kpc}$  we assume a flat rotation curve.

## CONCLUSION

Here we have presented novel HI observations of the galactic plane taken on the Green Bank Observatory's 20-meter telescope. By mapping the velocity of gas between  $0^\circ < l < 80^\circ$  using the TPM, we have shown that the rotation curve of our galaxy does not fall off like  $r^{-1/2}$  but stabilizes even at large distances from the galactic center. In comparison to more sophisticated maps of the Milky Way's rotation curve, our data is consistent.

These results suggest a large discrepancy in the amount of luminous matter present in our galaxy compared to the total mass. Such an empirical disagreement with theoretical expectations implies the existence of dark matter in large proportions. The mass of the dark matter halo of the Milky Way galaxy is known to be roughly  $5.4 \times 10^{11}$  solar masses, where the luminous matter of the galaxy is  $9 \times 10^{10}$  solar masses [6]. Rotation curves remain one of the most ideal methods of indirect observation of dark matter.

## ACKNOWLEDGMENTS

The Green Bank Observatory is a facility of the National Science Foundation operated under cooperative agreement by Associated Universities, Inc. The Green Bank 20-meter observations for this project were supported by Green Bank Observatory's Education and Public Outreach division. The Green Bank 20-

meter telescope is used as part of the Skynet Robotic Telescope Network, which operates out of the University of North Carolina at Chapel Hill and is supported by the National Science Foundation, North Carolina Space Grant, and the Mount Cuba Astronomical Foundation.

R. P. and H. J. acknowledge George Spagna, Michael Rodruck, Pedro Salas, and Will Armentrout for their assistance. Additionally, we acknowledge Python and its associated packages in Jupyter Lab and Wolfram Mathematica.

## REFERENCES

1. S. van den Bergh, *Astronom. Soc. Pacific* **111**, 657–660 (1999).
2. L. Baudis, *J. Phys. G: Nucl. Part. Phys.* **43** (2016).
3. V. C. Rubin, D. Burstein, J. W. Kent Ford, and N. Thonnard, *Astrophys. J.* **289**, 81–104 (1985).
4. A. Bosma, *Astrophys. J.* **86**, 1825–1846 (1981).
5. G. Bertone and D. Hooper, *Rev. Mod. Phys.* **90** (2016).
6. B. W. Carroll and D. A. Ostlie, *An Introduction to Modern Astrophysics* (Cambridge University Press, 2017).
7. L. Bergstrom, *New J. Phys* **11**, 105006 (2009).
8. S. Profumo, *An Introduction to Particle Dark Matter* (World Scientific, 2017).
9. R. Giovanelli and M. P. Haynes, *Astrophys. J.* **571**, L107–L111 (2002).
10. M. J. Reid, K. M. Menten, A. Brunthaler, X. W. Zheng, T. M. Dame, Y. Xu, Y. Wu, B. Zhang, A. Sanna, M. Sato, K. Hachisuka, Y. K. Choi, Immer, L. Moscadelli, K. L. J. Rygl, and A. Bartkiewicz, *Astrophys. J.* **783**, 14 (2014).
11. M. Honma, T. Nagayama, K. Ando, T. Bushimata, Y. K. Choi, T. Handa, T. Hirota, H. Imai, T. Jike, M. K. Kim, O. Kameya, N. Kawaguchi, H. Kobayashi, T. Kurayama, S. Kuji, N. Matsumoto, S. Manabe, T. Miyaji, K. Motogi, A. Nakagawa, et al., *Publ. Astron. Soc. Jpn.* **64** (2012).
12. M. Persic, P. Salucci, and F. Stel, *R. Astron. Soc.* **281**, 27–47 (1996).
13. G. Van Rossum and F. L. Drake, *Python 3 Reference Manual* (CreateSpace, Scotts Valley, CA, 2009).
14. Mathematica Version 13.0.0, Wolfram Research, Inc., Champaign, IL, 2021.
15. T. Kluyver, B. Ragan-Kelley, F. Pérez, B. Granger, M. Bussonnier, J. Frederic, K. Kelley, J. Hamrick, J. Grout, S. Corlay, P. Ivanov, D. Avila, Abdalla, and C. Willing, *Jupyter notebooks – A publishing format for reproducible computational workflows*, in *Positioning and Power in Academic Publishing: Players, Agents and Agendas*, edited by F. Loizides and B. Schmidt (IOS Press, 2016), pp. 87–90.
16. C. Moorman, *Spin flip transition of hydrogen in astrophysics*, Drexel University (2010).
17. Y. Sofue, *Publ. Astron. Soc. Jpn.* **69** (2017).
18. The value of the local standard of rest is not still considered to be exactly  $220 \text{ km s}^{-1}$ . The International Astronomical Union recommended that value decades ago, but the LSR is currently understood to be  $236 \pm 7 \text{ km s}^{-1}$  [20]. Using a value of  $220 \text{ km s}^{-1}$  allows us to compare our data directly to other surveys. Updating this value would shift our results uniformly.
19. D. Russeil, A. Zavagno, J. P. Mège, Y. Poulin, S. Molinari, and L. Cambresy, *Astron. Astrophys.* **601** (2017).
20. M. J. Reid, K. M. Menten, A. Brunthaler, X. W. Zheng, T. M. Dame, Y. Xu, Y. Wu, J. Li, N. Sakai, Y. Wu, K. Immer, B. Zhang, A. Sanna, Moscadelli, K. L. J. Rygl, A. Bartkiewicz, B. Hu, L. H. Quiroga-Nuñez, and H. J. van Langevelde, *Astrophys. J.* **885**, 18 (2019).
21. J. E. Gunn, G. R. Knapp, and S. D. Tremaine, *Astrophys. J.* **84**, 8 (1979).
22. L. Baudis, *Phys. Rev.* **94**, 262 (1954).

# A Simple Model for Understanding Cloud Diffusion on a Brown Dwarf

Joseph A. Landsittel<sup>a)</sup> and Ryan A. Coldren<sup>b)</sup>

*Department of Physics & Astronomy, University of Pittsburgh, 3941 O'Hara St., Pittsburgh, Pennsylvania 15260, USA*

<sup>a)</sup>Corresponding author: landsittel@pitt.edu

<sup>b)</sup>rac214@pitt.edu

**Abstract.** Brown dwarfs in the L-T spectral class transition commonly experience photometric variability due to the active formation/dissipation of clouds that rotate in and out of our view. Measurements of these photometric oscillations, such as their frequency and amplitude, may help constrain the physical parameters of observed brown dwarfs through their associations with aspects such as rotational period and surface temperature. However, measurements of these oscillations and their significance are obscured by the inclination angle of observed brown dwarfs relative to us. By creating a simplistic model of 2D cloud formation on the surface of a toy model brown dwarf, this paper aims to further explore the relationship between oscillation amplitude and inclination angle for cloudy brown dwarfs and finds agreement with the correlation found observationally between the two factors in Vos et al., 2017.

## INTRODUCTION

Brown dwarfs are substellar objects in a mass range  $0.012\text{-}0.075 M_{\odot}$  and surface temperature range  $<2400 \text{ K}$  (classified by the L, T, Y system; L being the hottest, Y being the coolest), with no theoretical lower limit for their surface temperature. However, the faintness of colder brown dwarfs, such as Y dwarfs typically below  $400 \text{ K}$ , makes their observation difficult, with the coldest known brown dwarf WISE J0855 being at  $250 \text{ K}$  [1]. Brown dwarfs form from the collapse of interstellar material, similar to a star, but do not gather enough mass to perform stable H to He fusion in their core. They instead undergo an insignificant amount of deuterium fusion due to their lower pressure/temperature threshold. Due to their severe lack of energy production, they slowly cool as they radiate their internal energy away [2, 3].

Brown dwarfs below  $2200 \text{ K}$  are often cool enough that atoms normally ionized in stars can form complex molecules. These molecules may even condense into a liquid/solid form on seed particles, creating clouds that stretch across the brown dwarf's atmosphere. Brown dwarfs transitioning between the L-T phase observationally are in a particularly active state of cloud formation and dissipation. These brown dwarfs are cool enough to support cloud condensation and have the more massive condensate grains, making the clouds eventually sink below the photosphere. The consequence is that "patchy" clouds constantly form, break up, and sink across the surface of L-T brown dwarfs [4, 5].

As a result of these clouds, photometrically, brown dwarfs appear to have an oscillating flux over time as a result of features rotating in/out of view and forming/dissipating during an observation [6]. This is especially true for L-T brown dwarfs due to their continual formation and dissipation of patchy clouds. Measuring the frequency and amplitude of these oscillations could provide valuable constraints on parameters for an observed brown dwarf, such as finding a potential relationship between the amplitude of oscillations and the spectral type of a brown dwarf.

A significant hurdle in this prospect, and one this paper aims to help resolve, is that the inclination angle of a brown dwarf relative to us drastically alters our photometric perception of surface features. Inclination potentially affects the flux received (or blocked) from clouds by changing their effective area, introducing limb darkening effects or changing how long they will stay in our field of view during one rotation [6]. By adopting a crude 2D toy model of a brown dwarf's surface cloud structure that includes limb darkening, convection, diffusion, and rotational effects, we attempt to find a tangible relationship between inclination angle and flux oscillation amplitude to explore this issue further. Additionally, we compare our results with the amplitude/inclination relation predicted in a previous paper by Vos et al., 2017.

## METHODS

We wish to describe the time evolution of clouds on a brown dwarf as a function of relevant physical phenomena: diffusion, convection, rotation, and the Coriolis effect. Though these forces have been included in brown dwarf atmosphere models in the past [7, 8], we are not aware of them having been isolated in the form we

present. The proposals we give here are intentionally simplified; our goal is to encapsulate the fundamental behavior of how these should act when superimposed on a brown dwarf without getting caught in an overcomplicated analysis.

The diffusion of any material across a surface is a well-studied phenomena, leaving us with no need to reinvent the proverbial wheel [9].

$$\frac{du}{dt} = D\nabla^2 u = \frac{D}{R^2 \sin(\theta)} [\partial_\theta(\sin(\theta)\partial_\theta u) + \partial_\varphi^2 u] = F_1(t, \theta, \varphi) \quad (1)$$

The time evolution of a gas in a space is governed by the Laplacian of that gas's concentration. In our case,  $u$  will describe the concentration of a "cloud seed" particulate (dust grains), and we will study the diffusion on the surface of the brown dwarf.  $R$  is the radius of the brown dwarf,  $\theta$  and  $\varphi$  are the latitudinal and longitudinal coordinates, respectively. We simulated with a normalized radius of  $R = 1$ .

Brown dwarfs are known to have cool, convective atmospheres composed of thin adiabatic layers [7]. There has been success rigorously modeling the subsequent dust formation and mixing in the atmosphere, with the field of *mixing length theory* [8]. Such hydrodynamic models capture the essentials of radiative transfer and energy transport in three dimensions.

We wish to encapsulate the qualitative behavior of dust mixing due to convection with a simple model that neglects the finer complexities of convection. In summary, this behavior is that an object with a strong convective outer layer tends to form granules across its surface; Schwarzschild defined these as the visible tops of rising convective elements [10]. We claim that dust particles rise within a granule with some constant frequency and that these granules are evenly distributed across the surface of the brown dwarf. We acknowledge the crude nature of such a claim while hoping that it does justice to convection to some approximation. Hence, due to convection,

$$\frac{du}{dt} = A \sin(\omega t + \theta + \varphi) = F_2(t, \theta, \varphi). \quad (2)$$

$A$  and  $\omega$  are the convection amplitude and timescales, respectively. This paper does not explore parameter dependencies; that is, we assume each force at play operates with weight on the same order of magnitude (i.e.,  $D = A = 1$ ,  $\omega = 1$ ). While this choice is able to reproduce essential behavior, a future direction could be to search for bifurcations as these are varied.

Rotation will result in the physical movement of dust particulate across longitude values, and the Coriolis effect should deflect longitudinal motion towards the equator. Rotation will have the strongest impact near the equator, where particulate must travel at a faster speed to keep up. In contrast, the Coriolis effect is zero at the equator.

To put this into mathematical language, consider the numerical representation of this phenomena. At any time step,  $t$ , rotation must move particulate from one longitude value into an adjacent longitudinal value. Thus, the change in particulate concentration at a given longitude is proportional to the adjacent longitude's particulate concentration and is inversely related to that longitude's own concentration

$$u[\varphi]_{t+\Delta t} = u[\varphi]_t + \gamma(\theta)(u[\varphi - \Delta\varphi]_t - u[\varphi]_t) \quad \gamma(\theta) = \frac{1}{30\sqrt{2\pi}} \exp\left[-\left(\frac{\theta - 90}{30}\right)^2\right] \quad (3)$$

where we took  $\gamma$  as a normal distribution maximized at the equator. We can complete this argument by converting to a continuous time domain and incorporating a similar argument for the form of the Coriolis effect [11]

$$\frac{du}{dt} = -\gamma(\theta)u_\varphi + [H(\theta - 90^\circ)\sin(\theta - 90^\circ) - H(90^\circ - \theta)\sin(90^\circ - \theta)]u_\theta = F_3(t, \theta, \varphi) \quad (4)$$

where  $H$  is the Heaviside function (which is incorporated to account for the difference in the Coriolis effect between the two hemispheres).

The resultant equation describing the time evolution of dust particulate is given by the superposition of Eqs. (1)-(4), that is,  $\frac{du}{dt} = \sum_i F_i(t, \theta, \varphi)$ , where each  $F_i$  is a distinct atmospheric force. The solution  $u(t, \theta, \varphi)$  outputs information regarding where particulate and clouds will accumulate. We simulate with a forward Euler numerical integration scheme [12]. Specifically, we solve an initial value problem starting with a uniform dispersion ( $u(0, \theta, \varphi) = u(0)$ ).

## CONCLUSIONS

The results of this approach are given in Fig. 1(a), with a video link to illustrate time dependence. Convection applies a visible forcing at each latitude, longitude coordinate. Rotation and the Coriolis force induce a global behavior of particulate movement around the sphere, with a buildup near the equator.

We wish to use our simulated predictions regarding the particulate and subsequent cloud concentrations in order to make claims regarding the relationship between viewing angle and light curve amplitude of a brown dwarf. To do this will require a few points of machinery to be explored. From our model, we can extract light curves resulting from any given set of latitude values. These are taken by assuming the cloud concentration at a point is inversely related to escaped light from the brown dwarf at that coordinate. Thus the simulation can equivalently be viewed as telling us the emissivity as a function of latitude, longitude, and time.

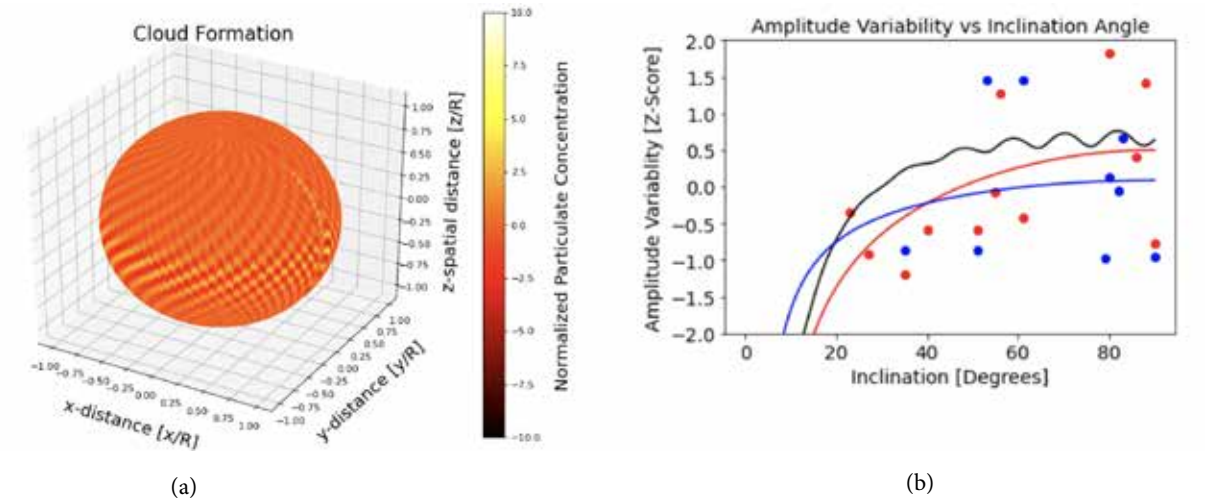
What an astronomer would see when viewing any stellar or large substellar object is a fraction of the light over the aligned hemisphere. However, integrating over a full  $180^\circ$  surface uniformly would be a misguided excursion neglecting the impact of limb darkening. We can summarize this effect in the following way: if the dot product of a normal vector to the surface at a given coordinate with a unit vector in the direction of the astronomer's line of sight is small, then a photon coming from that coordinate will have to travel through more atmosphere than an equivalent photon coming from a point where the dot product is 1 [13]. Hence, in extracting results, we take care to down weight the influence of the outer limbs of a surface of interest.

Figure 1(b) illustrates how the relationship our model predicts between amplitude variability and inclination compares with preexisting data. Before moving further, we will note our choice of normalization in using a z-score norm. We assume the variability in the light curve amplitudes to be loosely distributed as a Gaussian, and we report the number of standard deviations away from the mean the light curve amplitude is when viewed at each fixed inclination angle. This is a toy model that cannot reproduce light curves exactly, but we can normalize it to view a relative comparison with available data.

The presented curve fits are in the form suggested by Vos, et. al., 2017:

$$A = \alpha \sin(\theta) - \frac{\kappa}{\sin(\theta)}. \quad (5)$$

The key prediction of our model that comes with a reasonably strong observational justification is that observed amplitude variability is limited for brown dwarfs with a small angle of inclination to the observer. Notably, we are of the understanding that there is no observational evidence of a brown dwarf with both a small ( $< 20^\circ$ ) inclination angle and a non-negligible amplitude variability [6].



**FIGURE 1.** (a) A fixed time image of the simulation. The color corresponds to the number of standard deviations a given spatial coordinate is away from the mean particulate concentration. View the full simulation online at <https://www.youtube.com/watch?v=GrIyYdXcHaU>. (b) Amplitude variability for a brown dwarf plotted against inclination angle. The black curve shows the results of our simulation. The red data (and subsequent curve fit) refers to *Spitzer*  $36 \mu\text{m}$  detections. The blue data (and subsequent curve fit) correspond to *J*-band detections.

Our model provides a baseline explanation for these observations. The atmospheric forces at play in a brown dwarf result in cloud oscillations being greatest near the equator; hence, the resultant light curve from the equator exhibits the greatest variability. Limb darkening minimizes this effect if the brown dwarf is viewed at a small angle of inclination. In such a case, the light curve would exhibit minimal variability as clouds sit still at the poles.

Another explanation for the effect could potentially be provided from the Doppler effect. If the brown dwarf is viewed equator on (high inclination angle), then we would expect wavelength deviation from light across the brown dwarf, resulting in variability when viewing the brown dwarf in a specific band. Such a theory is beyond the scope of this model's capacity but has been explored by other researchers [14].

## ACKNOWLEDGMENTS

We wish to acknowledge the support and feedback provided by Dr. Carlos Badenes (University of Pittsburgh) throughout this project. We also thank Jacob Boomsma (University of Utah) for discussions on atmospheric science that contributed to the result.

## REFERENCES

1. K. L. Luhman, *Astrophys. J. Lett.* **786**(2), L18 (2014).
2. A. Franknoi and D. Morrison, *Astronomy* (12th Media Services, 2016).
3. A. Burrows and J. Liebert, *Rev. Mod. Phys.* **65**(2), 301–336 (1993).
4. P. A. Wilson, A. Rajan, and J. Patience, *Astron. Astrophys.* **566**, A111 (2014).
5. S. A. Metchev, A. Heinze, D. Apai, D. Flateau, J. Radigan, A. Burgasser, M. S. Marley, E. Artigau, P. Plavchan, and B. Goldman, *Astrophys. J.* **799**(2), 154 (2015).
6. J. M. Vos, K. N. Allers, and B. A. Biller, *Astrophys. J.* **842**(2), 78 (2017).
7. S. Mohanty, I. Baraffe, and G. Chabrier, *Proc. Int. Astron. Union* **239**(2), 197 (2006).
8. B. Freytag, F. Allard, H. G. Ludwig, D. Homeier, and M. Steffen, *Astron. Astrophys.* **513**, A19 (2010).
9. W. A. Strauss, *Partial Differential Equations: An Introduction*, 2nd ed. (Wiley, 2007).
10. M. Schwarzschild, *Astrophys. J.* **134**, 1 (1961).
11. J. R. Holton, *An Introduction to Dynamic Meteorology*, 4th ed. (Elsevier Academic Press, 2004).
12. A. I. Garcia, *Numerical Methods for Physics*, 2nd ed. (CreateSpace Independent Publishing Platform, 2017).
13. R. H. Brown, J. Davis, R. J. W. Lake, and R. J. Thompson, *Mon. Not. R. Astron. Soc.* **167**, 475 (1974).
14. É. Artigau, Variability of brown dwarfs, in *Handbook of Exoplanets*, edited by H. J. Deeg and J. A. Belmonte (Springer International Publishing, Cham, 2018), pp. 555–573.

# An Introduction to Quantum Computing

Ricco Venterea<sup>1, a)</sup> and Urbas Ekka<sup>2, b)</sup>

<sup>1)</sup>*Department of Astronomy, Cornell University, Ithaca, New York 14850, USA*

<sup>2)</sup>*Department of Mathematics, University of Minnesota, Twin Cities, Minnesota 55141, USA*

<sup>a)</sup>*Corresponding author: rvc38@cornell.edu*

<sup>b)</sup>*ekka0002@umn.edu*

**Abstract.** We present an overview of quantum computing, including relevant physics, processes, and applications. This includes describing the basic framework of the quantum bit, which serves as the foundation for the rest of this paper. We found rapid developments in quantum computing, which will have important consequences for future applications in scientific fields.

## INTRODUCTION

"[I] believe it's true that with a suitable class of quantum machines you could imitate any quantum system, including the physical world" [1]. With these words Richard Feynman ushered in a revolution. He shook off the shackles of classical computing and reached for the possibilities of quantum computing.

Quantum computing seeks to expand the typical computational power of classical computing. Classical computing is fundamentally based on 0s and 1s. Unlike quantum computing, these values are independent of any measurement. But due to this rigidity, classical computing has its limitations, especially in the realm of computational speed. Certain classical problems can be solved faster with quantum computers, although those problems rely on a small number of qubits to have any practical impact. To achieve such results, quantum computers implement quantum algorithms. As an example of this speedup, researchers demonstrated the power of quantum supremacy with a processor that took 200 seconds to make measurements of a quantum circuit, a process that would otherwise have taken a classical supercomputer 10,000 years [2].

There are numerous applications for quantum computing, as quantum algorithms abound in mathematical and physical applications. One example is factoring numbers. Classically, factoring numbers is computationally expensive. Shor's quantum algorithm does this at a much higher speed. Another example is cryptography, or more specifically, quantum key distribution (QKD). Even though public key cryptography incorporates some of the strongest encryptions out there, it still can provide only up to 30 years of security [3]. This level of security is fine for most industries, but for some more sensitive industries such as healthcare or defense, something like QKD that promises a longer life-time is optimal. Another example is the use of Grover's algorithm, a quantum search algorithm used to speed up an exhaustive subroutine (generally part of NP-complete problems).

## QUANTUM BITS

Quantum computing is probabilistic, which makes it vastly different from classical computing. Qubits now take on the role of classical bits. Indeed, it is these qubits that allow quantum computations to be performed. The state (or "status") of a qubit is composed of superpositions of pure states. These pure states form a basis for the system, so any new state of the system can be written in terms of a linear combination of the pure states. A measurement can be thought of as any experiment determining the state of electrons, photons, nuclei, or phonons [4–6]. When the measurement is made, the qubit takes on a value of 0 or 1 (the familiar classical bit), with a probability given by the initial state of the system [7]. Mathematically, prior to the measurement, there is some probability  $d_0^2$  of measuring 0 and probability  $d_1^2$  of measuring 1 such that [4]

$$d_0^2 + d_1^2 = 1 \quad (1)$$

It should be noted that  $d_0$  and  $d_1$  are the weights from the linear combination of the pure states of the system. The system can thus be written as

$$d_0|0\rangle + d_1|1\rangle \quad (2)$$

# Attend Your Zone Meeting this Year!



Zone meetings bring together students from SPS chapters within the same geographical area. These student led meetings are fun and memorable ways for physics and astronomy undergraduates to meet each other, present their research, and interact with practicing scientists!

To find out when and where your zone meeting will take place, connect with your (Associate) Zone Councilors at [www.spsnational.org/about/governance/national-council](http://www.spsnational.org/about/governance/national-council).

For more information about zone meetings or if your SPS chapter is interesting in hosting one, visit [www.spsnational.org/meetings/zone-meetings](http://www.spsnational.org/meetings/zone-meetings).



where

$$|0\rangle = \begin{pmatrix} 1 \\ 0 \end{pmatrix} \quad |1\rangle = \begin{pmatrix} 0 \\ 1 \end{pmatrix}$$

which resides in  $\mathbb{C}^2$ . When dealing with multiple qubits, the complex vector space grows exponentially according to  $2^n$ , where  $n \in \mathbb{N}$  [8].

## QUANTUM GATES

Quantum gates are operations on qubits. A measurement of the state of the qubit always gives  $|0\rangle$  or  $|1\rangle$ . So while the system starts with a probability distribution, it collapses to one of these two values after a measurement. Quantum gates for one qubit are represented as  $2 \times 2$  matrices. We present an example of the quantum X gate, which is similar to the NOT gate in classical computing.

$$\begin{bmatrix} 0 & 1 \\ 1 & 0 \end{bmatrix} |0\rangle = |1\rangle \quad \begin{bmatrix} 0 & 1 \\ 1 & 0 \end{bmatrix} |1\rangle = |0\rangle$$

When dealing with more than one qubit, the transformation matrix changes size, which is now  $2^n \times 2^n$ , where  $n$  is a positive integer. We provide a matrix representation of the CNOT gate, which is used in quantum entanglement [8].

$$\begin{bmatrix} 1 & 0 & 0 & 0 \\ 0 & 1 & 0 & 0 \\ 0 & 0 & 0 & 1 \\ 0 & 0 & 1 & 0 \end{bmatrix} |00\rangle = |00\rangle \quad \begin{bmatrix} 1 & 0 & 0 & 0 \\ 0 & 1 & 0 & 0 \\ 0 & 0 & 0 & 1 \\ 0 & 0 & 1 & 0 \end{bmatrix} |01\rangle = |01\rangle \quad \begin{bmatrix} 1 & 0 & 0 & 0 \\ 0 & 1 & 0 & 0 \\ 0 & 0 & 0 & 1 \\ 0 & 0 & 1 & 0 \end{bmatrix} |10\rangle = |11\rangle \quad \begin{bmatrix} 1 & 0 & 0 & 0 \\ 0 & 1 & 0 & 0 \\ 0 & 0 & 0 & 1 \\ 0 & 0 & 1 & 0 \end{bmatrix} |11\rangle = |10\rangle$$

## QUANTUM ENTANGLEMENT

Quantum entanglement is when the value of a qubit can be determined by measuring the state of a different qubit [8]. From a physical perspective, quantum entanglement can be described as when the state of a particle  $P_1$  depends on the state of another particle  $P_2$  and vice versa. Measuring the energy of  $P_1$  might give the value  $E_a$ , which would mean the energy of  $P_2$  is definitely  $E_b$ , or if the particle  $P_1$  has an energy of  $E_c$ ,  $P_2$  has an energy of  $E_d$  [9]. Thus, when the value of one qubit is known, the value of the other is also known [8]. This is incredibly useful in quantum computing, as entanglement drastically improves the processing speed.

## QUANTUM CIRCUITS

Much like using classical bits for classical computations, a collection of quantum bits is used for quantum computations. This collection is called a quantum register, with all qubits set in the initial state  $|0\rangle$ . A quantum circuit is thus a series of quantum gates that takes qubits as input from the quantum register [8]. Schematically, quantum gates are operations on quantum bits, with quantum circuits being this collection of operations to achieve an end goal. There are various quantum gates which can be ordered in several ways within quantum circuits.

## QUANTUM ANNEALING

There are also more specialized forms of quantum computing. One such example is quantum annealing, which is especially powerful in problems with low-energy solutions, such as optimization and sampling problems. There may be many local minima, so to ensure the global minimum is reached, the energy of the system is temporarily changed through an iterative process. An example of such a process is the quantum unconstrained binary optimization algorithm [10]. There are generally two steps in finding the global minimum. If the system's energy decreases, the

process is repeated. If the energy does not decrease, the process is not repeated right away but instead kept with some probability

$$P \propto \exp\left\{-\frac{\Delta E}{k_B T}\right\} \quad (3)$$

where  $\Delta E \equiv E_{final} - E_{initial}$ , with temperature  $T$  and Boltzmann constant  $k_B$ . As this process seeks to find the minimal energy, this corresponds to an energy state with minimal temperature  $T$ . Therefore, as the process is repeated, the temperature starts from a very high value, eventually approaching zero. When the temperature is zero, the energy is equal to the internal system's energy. So at the end of this process, the global minimum energy is found with a high degree of certainty and thus solves the optimization problem [11].

## CONCLUSION

Quantum computing utilizes qubits in place of its classical bit counterpart. The qubit is composed of the superposition of the pure states, and the quantum gates apply operations to these qubits. Collecting these gates together gives us a quantum circuit whose orientation is used to define the quantum algorithm. Furthermore, quantum entanglement between qubits and quantum annealing are utilized to maximize the efficiency of the system.

With Rigetti Computing proposing methods to rapidly improve quantum models, inching closer to overtaking classical computing in the realm of satellite image classification, and IonQ further developing frameworks to better simulate molecular interactions, we come closer and closer to the quantum world Richard Feynman imagined all those years ago [12, 13].

## REFERENCES

1. R. Feynman, "Simulating Physics with Computers," *Int. J. Theor. Phys.* **21**, 467–488 (1982), (keynote speech).
2. F. Arute, K. Arya, R. Babbush, D. Bacon, J. C. Bardin, R. Barends, R. Biswas, S. Boixo, F. G. S. L. Brandao, D. Buell, B. Burkett, Y. Chen, B. Chiaro, R. Collins, W. Courtney, A. Dunsworth, E. Farhi, B. Foxen, A. Fowler, C. Gidney, et al., *Nature* **574**, 505–510 (2019).
3. D. Stebila, M. Mosca, and N. Lütkenhaus, in *Quantum Communication and Quantum Networking*, edited by A. Sergienko, S. Pascazio, and P. Villoresi, QuantumComm (Springer, Naples, Italy, 2009), Vol. 36, pp. 283–296.
4. C. Bernhardt, *Quantum Computing for Everyone* (MIT Press, Cambridge, MA, 2019).
5. A. A. Wood, R. M. Goldblatt, R. E. Scholten, and A. M. Martin, *Phys. Rev. Research* **3**, 043174 (2021).
6. E. Berrios, M. Gruebele, D. Shyshlov, L. Wang, and D. Babikov, *J. Phys. Chem. A* **116**, 11347–11354 (2012).
7. R. Feynman, "The Concept of Probability in Quantum Mechanics," (Berkeley Symposium on Mathematical Statistics and Probability, 1951), pp. 533–541.
8. R. S. Sutor, *Dancing with Qubits: How Quantum Computing Works and How It Can Change the World* (Packt Publishing Ltd., Birmingham, UK, 2019).
9. D. J. Griffiths and D. F. Schroeter, *Introduction to Quantum Mechanics*, 3rd ed. (Cambridge University Press, 2018).
10. G. G. Guerreschi, preprint arXiv: 2101.07813 [quant-ph], 1–16 (2021).
11. B. K. Chakrabarti and A. Das, Transverse Ising model, glass and quantum annealing, in *Quantum Annealing and Related Optimization Methods* (Springer, 2005).
12. M. Henderson, J. Gallina, and M. Brett, *Quantum Mach. Intell.* **3** (2021), 10.1007/s42484-020-00034-6.
13. Y. Nam, J.-S. Chen, N. C. Pienti, K. Wright, C. Delaney, D. Maslov, K. R. Brown, S. Allen, J. M. Amini, J. Apisdorf, K. M. Beck, A. Blinov, Chaplin, M. Chmielewski, C. Collins, S. Debnath, K. M. Hudek, A. M. Ducore, Keesan, S. M. Kreikemeier, et al., *npj Quantum Inf.* **6** (2020), 10.1038/s41534-020-0259-3.

# On the Resonances of Coupled Qubit–Cavity Systems

Eashwar N. Sivarajan

Physics Department, Boston University, Boston, Massachusetts 02215, USA

Corresponding author: eashwar@bu.edu, eashwarnsivarajan@gmail.com

**Abstract.** We consider a system consisting of a qubit and a microwave transmission line that are coupled by a capacitor which, in turn, is modulated sinusoidally. The Unruh effect is the simultaneous production from vacuum of a pair of photons, one in the qubit and the other in the cavity. The dynamical Casimir effect is the production from vacuum of a pair of photons in the cavity. We analyze this qubit–cavity system and show that the system can be viewed as a pair of coupled quantum-mechanical oscillators and that both the Unruh effect and the dynamical Casimir effect are resonances of this coupled oscillator system. For the case where the cavity supports two propagating modes, in addition to the Unruh and dynamical Casimir effect at each of the supported modes, we predict a “paired Casimir effect,” where one photon is emitted in the cavity in each of two allowed modes, at the appropriate driving frequency. We also calculate analytical approximations to the driving frequencies for all three effects.

## INTRODUCTION

Quantum field theory predicts that a uniformly accelerating photodetector will detect photons in an electromagnetic vacuum which is termed the Unruh effect [1]. It also predicts that accelerating the mirror boundary of a cavity will result in the production of photon pairs in the cavity, which is termed the dynamical Casimir effect. Since the uniform acceleration required to observe the Unruh effect is very large,  $\approx 10^{20}$  m/s, following other researchers [2, 3], we consider the oscillatory analog of the Unruh effect where the photodetector is moved back and forth rapidly at gigahertz frequencies, resulting in (nonuniform) acceleration of similar magnitude. In this paper, we arrive at a unified analysis of photon production from an electromagnetic vacuum based on the oscillatory Unruh and dynamical Casimir effects.

We consider the qubit–cavity system analyzed by Blencowe and Wang [3] and shown in Fig. 1. According to the predictions of the oscillatory Unruh effect [2, 3], when the coupling capacitor is driven at the appropriate frequency, it will simultaneously produce a photon in both the qubit and the cavity. The photon generated in the qubit will cause a transition from the ground to the excited state. The photon in the cavity will excite one of the cavity modes determined by the energy/frequency of the photon. Since the boundary of the cavity is also oscillating, the dynamical Casimir effect [4], where a pair of photons is produced in the cavity while the qubit remains in the ground state, should be observed, albeit at a different driving frequency.

Following the methods in [3, 5] for the single-mode case, we can show that the quantum Hamiltonian for a transmission line supporting  $M$  modes is given by  $\hat{H}_{\infty} = \hat{H}_0 + \hat{H}_1$ , where

$$\hat{H}_0 = \frac{E_1 - E_0}{2} \sigma_z + \hbar \sum_{m=1}^M \omega_m \hat{a}_m^\dagger \hat{a}_m, \quad \text{and} \quad \hat{H}_1 \equiv \sum_{m=1}^M h_m = \sum_{m=1}^M f_m(t) (\sigma^+ + \sigma^-) (\hat{a}_m - \hat{a}_m^\dagger). \quad (1)$$

Here,  $E_0$  and  $E_1$  are the two lowest energy levels of the qubit,  $\omega_m$  is the frequency of cavity mode  $m$ ,  $\hat{a}_m$  and  $\hat{a}_m^\dagger$  are ladder operators, and  $f_m(t) = -i\hbar g_m(1 + z(t))$ , where  $z(t)$  is the changing thickness between the capacitor plates, and  $g_m$  is the coupling coefficient between the qubit and cavity mode  $m$ . The detailed derivation of (1) can be found in [6]. Following [5], we have assumed that the boundary conditions on the qubit flux and cavity modes are such that the cavity modes are decoupled.

The cavity-mode terms in the Hamiltonian (1) are those of a parametric amplifier, and this analogy has been used to realize the dynamical Casimir effect using microwave cavity resonators with tunable lengths. However, we will show in our model (Fig. 1) that the combined qubit-cavity system is more analogous to a driven harmonic oscillator with the varying capacitance providing the driving term.

## TIME-DEPENDENT PERTURBATION SOLUTION

We view  $\hat{H}_0$  as the unperturbed Hamiltonian and  $\hat{H}_1$  as a time-dependent perturbation. If we denote the cavity state as  $\mathbf{n}_k = (n_{k_1}, n_{k_2}, \dots, n_{k_M})$ , the state of the unperturbed system can be represented by  $|q, \mathbf{n}_k\rangle = |q, n_{k_1}, n_{k_2}, \dots, n_{k_M}\rangle$ , where  $q \in \{g, e\}$  denotes the state of the qubit (ground or excited) and  $n_{k_i} \geq 0$  is the total number of photons in cavity mode  $k_i$ . Thus,  $N = \sum_i n_{k_i}$  is the number of photons in the cavity.

Denoting the state of the perturbed system as  $\sum c_{q, \mathbf{n}_k} |q, \mathbf{n}_k\rangle$ , using standard time-dependent perturbation theory (see, e.g., Eq. (5.5.17) of [7]), we have the following differential equations for the  $c_{q, \mathbf{n}_k}$ .

$$\dot{c}_{q, \mathbf{n}_k} = -\frac{i}{\hbar} \sum_{q'} \sum_{\mathbf{n}'_k} \sum_{m=1}^M \left( c_{q', \mathbf{n}'_k} \langle q, \mathbf{n}_k | h_m | q', \mathbf{n}'_k \rangle \right) e^{i(E_{q', \mathbf{n}'_k} - E_{q, \mathbf{n}_k})t/\hbar}. \quad (2)$$

By the definition of the ladder operators  $\hat{a}_m$  and  $\hat{a}_m^\dagger$ , and the operators  $\sigma^+$  and  $\sigma^-$ , we can show that

$$h_m |g, \mathbf{n}_k\rangle = f_m \sqrt{n_{k_m}} |e, \mathbf{n}_k - \mathbf{1}_m\rangle - f_m \sqrt{n_{k_m} + 1} |e, \mathbf{n}_k + \mathbf{1}_m\rangle \quad (3)$$

$$\text{and } h_m |e, \mathbf{n}_k\rangle = f_m \sqrt{n_{k_m}} |g, \mathbf{n}_k - \mathbf{1}_m\rangle - f_m \sqrt{n_{k_m} + 1} |g, \mathbf{n}_k + \mathbf{1}_m\rangle, \quad (4)$$

where  $\mathbf{1}_m$  is the vector whose  $m$ th component is unity, and the other components are zero.

We also know that

$$E_{g, \mathbf{n}_k} = E_0 + \hbar \sum_m \omega_m \left( n_{k_m} + \frac{1}{2} \right), \quad \text{and} \quad E_{e, \mathbf{n}_k} = E_1 + \hbar \sum_m \omega_m \left( n_{k_m} + \frac{1}{2} \right). \quad (5)$$

Thus, defining  $\Omega = (E_1 - E_0)/\hbar$ ,

$$E_{e, \mathbf{n}_k \pm \mathbf{1}_m} - E_{g, \mathbf{n}_k} = \hbar(\Omega \pm \omega_m), \quad \text{and} \quad E_{g, \mathbf{n}_k \pm \mathbf{1}_m} - E_{e, \mathbf{n}_k} = \hbar(-\Omega \pm \omega_m). \quad (6)$$

Plugging these into (2), we get

$$\begin{aligned} \dot{c}_{g, \mathbf{n}_k} &= \sum_{m=1}^M c_{e, \mathbf{n}_k + \mathbf{1}_m} f_m \sqrt{n_{k_m} + 1} e^{it(\Omega + \omega_m)} - c_{e, \mathbf{n}_k - \mathbf{1}_m} f_m \sqrt{n_{k_m}} e^{it(\Omega - \omega_m)} \\ \dot{c}_{e, \mathbf{n}_k} &= \sum_{m=1}^M c_{g, \mathbf{n}_k + \mathbf{1}_m} f_m \sqrt{n_{k_m} + 1} e^{it(-\Omega + \omega_m)} - c_{g, \mathbf{n}_k - \mathbf{1}_m} f_m \sqrt{n_{k_m}} e^{it(-\Omega - \omega_m)}. \end{aligned} \quad (7)$$

Since we are dealing with weak powers, we neglect instances where three or more photons propagate in the cavity. Now, the state of the system can be written as  $|q, \mathbf{0}\rangle$  when there are no photons in the cavity,  $|q, \mathbf{1}_n\rangle$  when there is one photon in mode  $k_n$ ,  $|q, \mathbf{2}_n\rangle$  when there are two photons in mode  $k_n$ , and  $|q, \mathbf{1}_{m,n}\rangle$  when there is one photon in each of the modes  $k_m$  and  $k_n$ . (Here,  $\mathbf{0} = (0, \dots, 0)$ ,  $\mathbf{2}_n = \mathbf{1}_n + \mathbf{1}_n$ , and  $\mathbf{1}_{m,n} = \mathbf{1}_m + \mathbf{1}_n$ .)

We can now write our differential equations for  $M$  allowed modes of propagation:

$$\begin{aligned} \dot{c}_{g, \mathbf{0}} &= \sum_{m=1}^M f_m c_{e, \mathbf{1}_m} e^{it(\Omega + \omega_m)}, \quad \dot{c}_{g, \mathbf{2}_n} = -f_n \sqrt{2} c_{e, \mathbf{1}_n} e^{it(\Omega - \omega_n)}, \quad n \in [1, M] \\ \dot{c}_{e, \mathbf{1}_n} &= f_n \sqrt{2} c_{g, \mathbf{2}_n} e^{it(-\Omega + \omega_n)} - f_n c_{g, \mathbf{0}} e^{it(-\Omega - \omega_n)} + \sum_{m \neq n} f_m c_{g, \mathbf{1}_{n,m}} e^{it(-\Omega + \omega_m)}, \quad n \in [1, M] \\ \dot{c}_{g, \mathbf{1}_{n,m}} &= -f_m c_{e, \mathbf{1}_n} e^{it(\Omega - \omega_m)} - f_n c_{e, \mathbf{1}_m} e^{it(\Omega - \omega_n)}, \quad n, m \in [1, M], m \neq n. \end{aligned} \quad (8)$$

## RESONANCES FOR TWO PROPAGATION MODES

We consider the case where only two modes propagate in the cavity ( $M = 2$ ) and write the Fock states as  $|q, n_{k_1}, n_{k_2}\rangle$ . We set the driving term  $z(t) = 0$  in order to find the homogeneous solution to Eq. (8), which will identify the resonance frequencies of the system. In turn, we can then determine the driving frequency to excite a specific resonance.

Taking the Fourier transform of (8), we get

$$i\omega C_{g00}(\omega) = g_1 C_{e10}(\omega - \Omega - \omega_1) + g_2 C_{e01}(\omega - \Omega - \omega_2) \quad (9)$$

$$i\omega C_{e10}(\omega) = g_1 \sqrt{2} C_{g20}(\omega + \Omega - \omega_1) - g_1 C_{g00}(\omega + \Omega + \omega_1) + g_2 C_{g11}(\omega + \Omega - \omega_2) \quad (10)$$

$$i\omega C_{g20}(\omega) = -g_1 \sqrt{2} \bar{C}_{e10}(\omega - \Omega + \omega_1) \quad (11)$$

$$i\omega C_{g11}(\omega) = -g_2 C_{e10}(\omega - \Omega + \omega_2) - g_1 C_{e01}(\omega - \Omega + \omega_1). \quad (12)$$

(We have omitted the equations for  $C_{e01}$  and  $C_{g02}$ .) We use (9), (11), and (12) to substitute for  $C_{g00}$ ,  $C_{g20}$ , and  $C_{g11}$  in (10) to get

$$\left( \omega - \frac{g_1^2}{\omega + \Omega + \omega_1} - \frac{2g_1^2}{\omega + \Omega - \omega_1} - \frac{g_2^2}{\omega + \Omega - \omega_2} \right) C_{e10}(\omega) = g_1 g_2 C_{e01}(\omega + \omega_1 - \omega_2) \left( \frac{1}{\omega + \Omega + \omega_1} + \frac{1}{\omega + \Omega - \omega_2} \right). \quad (13)$$

Simplifying, we get an equation of the form

$$F(\omega, \omega_1, \omega_2, \Omega, g_1, g_2) C_{e10}(\omega) = g_1 g_2 C_{e01}(\omega + \omega_1 - \omega_2) [\omega + \Omega - \omega_1], \quad (14)$$

where  $F$  is a polynomial of degree 4 in  $\omega$ . Similarly,

$$F(\omega, \omega_2, \omega_1, \Omega, g_2, g_1) C_{e01}(\omega) = g_2 C_{e10}(\omega + \omega_2 - \omega_1) [\omega + \Omega - \omega_2]. \quad (15)$$

From (15) we substitute for  $C_{e01}$  into (14) to get an equation of the form

$$F(\omega, \omega_1, \omega_2, \Omega, g_1, g_2) F(\omega + \omega_1 - \omega_2, \omega_2, \omega_1, \Omega, g_2, g_1) C_{e10}(\omega) = g_1^2 g_2^2 C_{e10}(\omega) [(\omega + \Omega - \omega_1)(\omega + \Omega + \omega_1 - 2\omega_2)]. \quad (16)$$

The l.h.s. has terms of order  $g_1^2$  and  $g_2^2$ . Therefore, for small  $g_1$  and  $g_2$  we can neglect the  $g_1^2 g_2^2$  term on the right and conclude that the resonance frequencies for  $c_{e10}(t)$  are among the zeroes of  $F(\omega, \omega_1, \omega_2, \Omega, g_1, g_2)$  and  $F(\omega + \omega_1 - \omega_2, \omega_2, \omega_1, \Omega, g_2, g_1)$ . If we consider the  $g_1^2$  and  $g_2^2$  terms as perturbations, the unperturbed zeroes of  $F(\omega, \omega_1, \omega_2)$  are  $0, -\Omega - \omega_1, -\Omega + \omega_1$ , and  $-\Omega + \omega_2$ , and hence those of  $F(\omega + \omega_1 - \omega_2, \omega_2, \omega_1)$  are  $\omega_2 - \omega_1, -\Omega - \omega_1, -\Omega + 2\omega_2 - \omega_1$ , and  $-\Omega + \omega_2$ . Therefore, the six unique possible resonance frequencies for the unperturbed  $|e10\rangle$  are

$$\omega_{R,e10} \in \{0, \omega_2 - \omega_1, -\Omega + \omega_1, -\Omega - \omega_1, -\Omega + \omega_2, -\Omega + 2\omega_2 - \omega_1\}. \quad (17)$$

The “zero” frequency component corresponds to steady growth of amplitude, and we should drive the system to excite this resonance. Considering (10), or its time-domain version from (8), the  $c_{g,0}$  dominates the r.h.s. as the other terms are small in comparison. Therefore, the driving frequency of the excitation,  $z(t)$ , in order to trigger resonance at  $\omega_{R,e10}$  is given by

$$\omega_{d,e10} = \omega_{R,e10} + \Omega + \omega_1 \in \{\Omega + \omega_1, \Omega + \omega_2, 2\omega_1, 0, \omega_1 + \omega_2, 2\omega_2\}. \quad (18)$$

The actual resonance frequencies will be close to these unperturbed values, and we can solve for them numerically. To find an analytical approximation to the resonance and driving frequencies for nonzero  $g_1, g_2 \ll \Omega, \omega_1, \omega_2$ , we use the perturbation series method: We assume the solutions to  $F(\omega, \omega_1, \omega_2, \Omega, g_1, g_2) = 0$  and  $F(\omega + \omega_1 - \omega_2, \omega_2, \omega_1, \Omega, g_2, g_1) = 0$  are of the form  $x_{00} + x_{10}g_1 + x_{01}g_2 + x_{20}g_1^2 + x_{02}g_2^2 + x_{11}g_1g_2$ , expand the polynomials to second order, equate the coefficients of  $g_1, g_2, g_1^2, g_2^2, g_1g_2$  to zero, and solve for the  $x_{ij}$ 's. By this method we find that the approximate driving frequency for steady resonance of the  $|e01\rangle$  state is

$$\omega_{d,Unruh} = \Omega + \omega_1 + \frac{3\Omega + \omega_1}{\Omega^2 - \omega_1^2} g_1^2 + \frac{1}{\Omega - \omega_2} g_2^2. \quad (19)$$

At this driving frequency, we expect simultaneous production of pairs of photons in the qubit and in the cavity with energy  $\hbar\omega_1$ , and the probability of this pair production steadily increases with time. In other words, this is the driving

frequency for observing the Unruh effect at  $\omega_1$ .

The possible resonance frequencies for  $|g20\rangle$  are obtained by shifting those of  $|e10\rangle$  by  $(\Omega - \omega_1)$  from (11):

$$\omega_{R,g20} \in \{\Omega - \omega_1, \Omega + \omega_2 - 2\omega_1, 0, -2\omega_1, \omega_2 - \omega_1, 2(\omega_2 - \omega_1)\}. \quad (20)$$

Now, substituting (10) in (11), we see that the possible driving frequencies for resonance of this state are obtained by adding  $2\omega_1$  to these values, equivalent to adding  $\Omega + \omega_1$  to the resonance frequencies of  $|e01\rangle$ . The perturbation series approximations are also obtained using this shift. Hence,

$$\omega_{d,Casimir} = 2\omega_1 - \frac{2}{\Omega - \omega_1} g_1^2. \quad (21)$$

The driving frequency for the dynamical Casimir effect is unaffected by the presence of the second mode, up to the accuracy of the perturbation approximation. This is unlike the Unruh driving frequency which was altered by the presence of the second cavity mode.

Finally, we consider the  $|g11\rangle$  state. The resonance frequencies are obtained by shifting those of  $|e10\rangle$  by  $(\Omega - \omega_2)$  from (12):

$$\omega_{R,g11} \in \{\Omega - \omega_2, \Omega - \omega_1, \omega_1 - \omega_2, -\omega_1 - \omega_2, 0, \omega_2 - \omega_1\}. \quad (22)$$

Substituting (10) in (12), we see that the driving frequencies are obtained by adding  $\omega_1 + \omega_2$  to these, indeed giving us the same possible unperturbed driving frequencies as for the  $|e10\rangle$  and  $|g20\rangle$  states.

Specifically,  $\omega_1 + \omega_2$  is the driving frequency for steady resonance of the  $|g11\rangle$  state. At this driving frequency, a pair of photons is produced simultaneously in the cavity, one each at  $\omega_1$  and  $\omega_2$ . Generalizing, if the cavity supports  $M$  modes, then we have additional resonances for the  $|e1_{m,n}\rangle$  mode for  $\omega_d = \omega_m + \omega_n$ ,  $m, n \in [1, M]$ . Since the case  $m = n$  corresponds to the dynamical Casimir effect, we may term this the *paired Casimir effect*. There is no conceptual difficulty in allowing for a continuum of modes: we expect to see the paired Casimir effect at driving frequencies  $\omega_d$  that satisfy  $\omega_d = \omega_m + \omega_n$ , where  $\omega_m$  and  $\omega_n$  are any two allowed modes.

On the same lines as above, we find that the driving frequency for the steady resonance of the  $|g11\rangle$  state corresponding to the paired Casimir effect is

$$\omega_{d,paired\ Casimir} = \omega_1 + \omega_2 + \frac{1}{-\Omega + \omega_1} g_1^2 + \frac{1}{-\Omega + \omega_2} g_2^2. \quad (23)$$

## Numerical Results for the Two-Mode Case

For strong coupling, say,  $g_1, g_2 \sim 0.1$ , the driving frequencies obtained by our perturbation approximation are significantly different from the unperturbed values. We refer the reader to [6] for some numerical results to verify their accuracy. Here, we assume weak coupling coefficients,  $g_1 = g_2 = 0.01$ . In this case, the resonance and driving frequencies are negligibly different from their unperturbed values. Despite the weak coupling, we will see that all three effects can be clearly observed.

In Fig. 2, we plot the probabilities for each of the cavity states to illustrate the Unruh effect at  $\omega_1$ . We can see that the probability of  $|e10\rangle$  approaches that of the starting state  $|g00\rangle$ . The probabilities of the other states are negligible. Next, we plot the probabilities for each of the cavity states to illustrate the dynamical Casimir effect at  $\omega_1$  in Fig. 3(a). This is orders of magnitude weaker than the Unruh effect and can be explained as follows. The initial condition is  $c_{g00}(0) = 1$ , and this is the only driving term for both effects. From Eq. (10), we can see that the amplitude of the  $c_{e10}$  state which corresponds to the Unruh effect is linear in the coupling coefficient  $g_1$ , whereas by combining Eqs. (11) and (10) we see that the amplitude of the  $c_{g20}$  state is quadratic in the coupling coefficient  $g_1$ . Since we assumed  $g_1 = 0.01$ , we expect the relative state probability for the dynamical Casimir effect to be four orders of magnitude smaller than that of the oscillatory Unruh effect, and this is borne out by our numerical results.

Finally, we plot the probabilities for each of the cavity states to illustrate the paired Casimir effect at  $\omega_1$  and  $\omega_2$  in Fig. 3(b). This effect is also orders-of-magnitude weaker than the Unruh effect but similar in strength to the dynamical Casimir effect, which can be understood by reference to Eqs. (12) and (10).

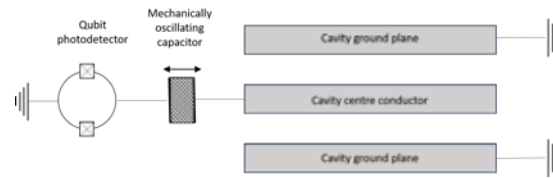


**FIGURE 1.** System model based on [3], consisting of a qubit photodetector and microwave cavity or transmission line coupled by a mechanically oscillating capacitor.

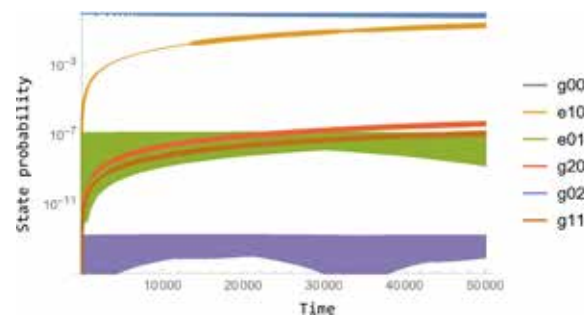


**FIGURE 2.** The time evolution of the state probabilities  $|c_{q,n}(t)|^2$  for  $\omega_1 = 9\pi$ ,  $\omega_2 = 10\pi$ ,  $\Omega = 6\pi$ ,  $g_1 = g_2 = 0.01$ , and  $\omega_d = 15\pi$ , which corresponds to the Unruh effect at  $\omega_1$ , which is clearly observed.

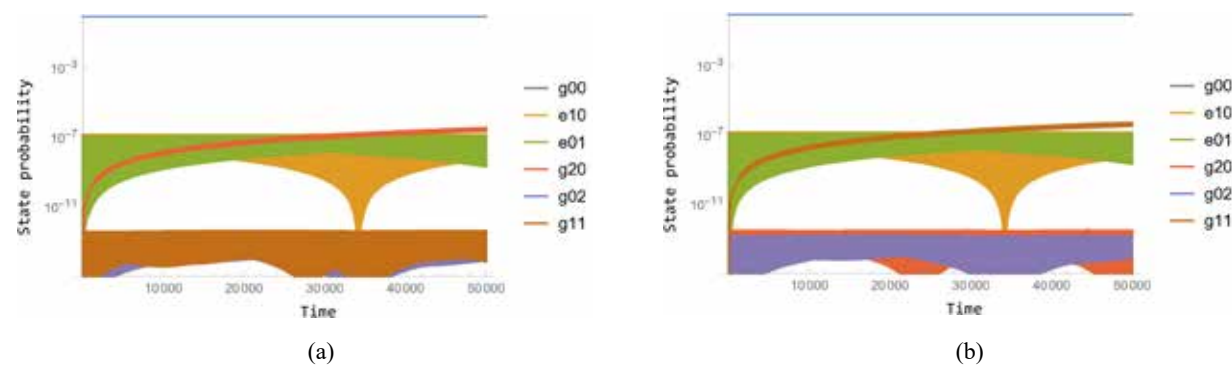


**FIGURE 3.**

- (a) The time evolution of the state probabilities  $|c_{q,n}(t)|^2$  for  $\omega_1 = 9\pi$ ,  $\omega_2 = 10\pi$ ,  $\Omega = 6\pi$ ,  $g_1 = g_2 = 0.01$ , and  $\omega_d = 18\pi$ , which corresponds to the dynamical Casimir effect at  $\omega_1$ : there is a non-negligible probability of occupying the state  $|g20\rangle$ .
- (b) The time evolution of the state probabilities  $|c_{q,n}(t)|^2$  for  $\omega_1 = 9\pi$ ,  $\omega_2 = 10\pi$ ,  $\Omega = 6\pi$ ,  $g_1 = g_2 = 0.01$ , and  $\omega_d = 19\pi$ , which corresponds to the paired Casimir effect at  $\omega_1$  and  $\omega_2$ : there is a non-negligible probability of occupying the state  $|g11\rangle$ .

## CONCLUSIONS

We neglected states with three or more photons and analytically found the driving frequencies that would result in the oscillatory Unruh and dynamical Casimir effects for a cavity supporting two modes. In both cases we derived analytical approximations to the driving frequencies necessary to observe the oscillatory Unruh and dynamical Casimir effects. For a multimode cavity, we predicted a new paired Casimir effect where a photon is emitted in each of two different modes of the cavity.

We did not make any assumption as to the rapidity of oscillations of the coupling capacitor. Hence, our model predicts that the oscillatory Unruh and dynamical Casimir effects merely reflect the resonances of the coupled qubit–transmission line, and no relativistic effects appear to be involved. Of course, building cavities at lower than microwave frequencies is probably unfeasible.

## ACKNOWLEDGMENTS

This work was done at the physics department of Dartmouth College in Hanover, New Hampshire. I sincerely thank my senior honors thesis advisor, Professor Miles Blencowe, Department of Physics, Dartmouth College, for his guidance and encouragement throughout this work.

## REFERENCES

1. W. G. Unruh, Phys. Rev. D **14**, 870–892 (1976).
2. H. Wang, M. P. Blencowe, C. M. Wilson, and A. J. Rimberg, Phys. Rev. A **99**, 053833 (2019).
3. M. P. Blencowe and H. Wang, Philos. Trans. R. Soc. London, Ser. A **378** (2020).
4. V. V. Dodonov, J. Phys. Conf. Ser. **161** (2009).
5. A. Parra-Rodriguez, E. Rico, E. Solano, and I. L. Egusquiza, Quantum Sci. Technol. **3** (2018).
6. E. N. Sivarajan, *On the Resonances of Coupled Qubit-Cavity Systems*, Senior honors thesis, Dartmouth College (2021).
7. J. J. Sakurai and J. Napolitano, *Modern Quantum Mechanics*, 2nd ed. (Cambridge University Press, 2017).

# 100 YEARS OF MOMENTUM

Join us for  $\Sigma\Pi\Sigma$ 's Centennial – the 2022 Physics Congress.  
100 Years of Momentum. An interactive meeting designed for undergraduate physics and astronomy majors.

**OCTOBER 6-8, 2022 | WASHINGTON, D.C.**



[sigmapisigma.org/congress/2022](https://sigmapisigma.org/congress/2022)



# Using $\gamma\gamma$ -Coincidence Spectroscopy to Identify Natural Radiation in Soils Near the Mississippi River

Pranjal Singh,<sup>1, a)</sup> Daniel Valmassei,<sup>1</sup> Anthony Kuchera,<sup>1</sup> and Ben Crider<sup>2</sup>

<sup>1)</sup>Department of Physics, Davidson College, Davidson, North Carolina 28035, USA

<sup>2)</sup>Department of Physics and Astronomy, Mississippi State University, Mississippi State, Mississippi 39762, USA

<sup>a)</sup>Corresponding author: prsingh@ davidson.edu

**Abstract.** Naturally radioactive nuclides present in soils contain background radiation that humans are exposed to every day. Previous research suggests that there are high background radiation areas (HBRAs) caused by climate, geography, wind, and water currents that accumulate a higher concentration of these radionuclides. An investigation of the Nile Delta confirms the presence of minerals rich in U and Th from monazite and zircon, further suggesting that certain locations have a higher concentration of these radionuclides. The present work is a search for monazite in Great River Road State Park, near the Mississippi River. The acquired samples were measured with a low-background NaI(Tl) spectrometer and digital data acquisition system. Using  $\gamma\gamma$ -coincidence spectroscopy to reduce background radiation, we were able to apply coincidence gates of known gamma-ray energies originating from  $^{238}\text{U}$  and  $^{232}\text{Th}$  decay chains to identify the presence of the radionuclides in the soil samples. From our results, we confirmed that there is an accumulation of minerals containing  $^{238}\text{U}$  and  $^{232}\text{Th}$  near the river. Our next steps will focus on calculating activities for quantitative results and collecting samples from an extended region along the river.

## INTRODUCTION

Water and air currents dictate accumulation of minerals around the shores of rivers, which results in a nonuniform spread of minerals containing naturally radioactive nuclides that contribute to the outdoor terrestrial natural radiation. Most soils have some amount of natural radionuclides such as  $^{40}\text{K}$ ,  $^{238}\text{U}$ ,  $^{235}\text{U}$ , and  $^{232}\text{Th}$ , that humans are exposed to every day.<sup>1</sup> A previous study by Mubarak et al. determined the Nile Delta near Rosetta Beach in Egypt to be a high background radiation area (HBRA) for deposits of beach placer or "black sand," which contains concentrations of monazite and zircon minerals along with a few others.<sup>1</sup> Monazite is a rare earth element mineral. Due to its high resistance to weathering, it can mostly be found in sedimentary matter and is valued for its thorium content.<sup>2</sup> The monazite that we are concerned with is fluvial monazite, found in rivers. Monazite has the highest concentration at the lower levels of the matter left behind by a river (alluvium), but some of it can continue downstream. If this alluvium contains gravel, then the monazite can get trapped between the spaces in the gravel; however, in many cases most of the monazite contributes downstream.<sup>3</sup>

As per geological reports, the largest concentrations of radioactive nuclides near the Mississippi Gulf Coast and associated offshore islands are found in the beach sands, with monazite being the most frequent mineral found.<sup>4</sup> The attributes of monazite are indicative of a formation in metamorphic rocks and the grade of metamorphism governs the concentration of thorium in the mineral,<sup>5</sup> but it is also said to contain a presence of uranium. This study investigates the formation of radionuclides in soil of Great River Road State Park, near the Mississippi River, for an exploration into the presence of monazite.

## EQUIPMENT AND METHODS

The setup for this investigation used two NaI(Tl) detectors (Scionix model 152AS102/5M-E2-X) each consisting of a cylindrical NaI(Tl) scintillation crystal with a diameter and height of 152 mm and 102 mm, respectively, with a stainless steel housing. The crystals were coupled with a low-background ET9390 photomultiplier tube (PMT), 127 mm in diameter, and a quartz optical window, to yield a low background radiation. The detectors faced each other at a distance of 8 cm and were enclosed by lead to reduce background radiation, as seen in Fig. 1 and Fig. 2. The enclosure consists of six 2-inch-thick lead bricks on the front and back and a lead 0.75-inch-thick slab on the top and bottom.

The detectors were biased with voltages of approximately 700 V and a preamplifier which was powered by +5 V. The data acquisition and processing system was XIA Pixie-Net, a multichannel digital spectrometer designed for high-precision coincidence spectroscopy by detector signal digitization, waveform capture, pulse height measurement, time stamping, online pulse shape analysis with 12-bit resolution, and 250 Megasamples per second pulse processor. The Pixie-Net software is managed by a collection of C/C++ programs. All collected data was analysed using the ROOT data analysis framework to obtain the presented histograms.<sup>6</sup>



FIGURE 1: Two NaI(Tl) detectors placed 8 cm apart with a sample.



FIGURE 2: Lead enclosure of the detectors for low-background counting setup.

Five calibration sources ( $^{137}\text{Cs}$ ,  $^{60}\text{Co}$ ,  $^{57}\text{Co}$ ,  $^{54}\text{Mn}$ ,  $^{22}\text{Na}$ ) were used for the conversion from multichannel analyzer (MCA) spectrum to energy. Each calibration source was measured for 5 minutes, and their MCA values were extracted by fitting the peaks with Gaussian distributions using ROOT to calculate a slope and offset from known gamma-ray energies. The energy resolution of each of the detectors, determined using the full width at half maximum divided by the actual value (661.7 keV) of  $^{137}\text{Cs}$ , was approximately 7%.

Two sets of soil samples (samples A and B) were collected in a few steps proximity of each other at a location off the trails in the Great River Road State Park. The exact location can be seen in Fig. 3. After collection the samples were dried and sealed in plastic bottles, see Fig. 1. Data for each sample was collected for 24 hours. The laboratory background, with no sample and bottle, was also measured for the same duration.

Coincidence spectroscopy was used to reduce background radiation further and identify the nuclides in the samples. To confirm the presence of  $^{232}\text{Th}$  and  $^{238}\text{U}$ , we applied coincidence gates from a study by Tillett et al.,<sup>7</sup> where coincidence gates represent the energy of a specific state into which other excited states transition. The coincidence gates for  $^{232}\text{Th}$  and  $^{238}\text{U}$  are extracted from the  $\beta$  decays of  $^{208}\text{Tl}$  to  $^{208}\text{Pb}$  and  $^{214}\text{Bi}$  to  $^{214}\text{Po}$ , respectively, which can be seen in Fig. 4. It is important to note that  $^{208}\text{Tl}$  and  $^{214}\text{Bi}$  are not direct byproducts of  $^{232}\text{Th}$  and  $^{238}\text{U}$  but are products after numerous  $\alpha$  and  $\beta$  decays. The  $\gamma$  rays originate from the transition of the first excited state to the ground state, where there are multiple transitions feeding into the first excited state by higher states from the  $\beta$  decays. Figures 5 and 6 present all events that fall within the 500-ns coincidence window. This coincidence window was applied in software to only keep events in which both detectors measured gamma rays. The energy gate is applied to one detector, then a 1-D histogram of all events from the other detector that come in coincidence with that gate is plotted to identify the radionuclide. To ensure that our detector is able to measure  $^{232}\text{Th}$  and  $^{238}\text{U}$  and to make certain that the known coincidence gates (2614 keV and 609 keV) provide the expected results, we tested samples known to contain  $^{232}\text{Th}$  and  $^{238}\text{U}$ . Our results reflected similar findings to Tillett et al. of activities of thorium and uranium in environmental samples. With this method verified, we applied the same approach to the soil samples.<sup>7</sup>



FIGURE 3: Map of Great River Road State Park with marker at (33°49'48.0"N, 91°03'00.0"W) where samples were taken.

## RESULTS

The 2-D histograms shown in Figs. 5 and 6 present all events in coincidence from both detectors. For coincidence gating, we looked specifically for vertical bands, indicating a particular energy in one detector; the diagonal bands represent Compton scattering and any other events in which an incident gamma ray deposits some of its energy into one detector and the remaining in the other. By referencing a background 2-D coincidence histogram, we were able to determine that the vertical band closer to 500 keV is seen consistently in all data. The 609-keV and 2614-keV gates presented in the 2-D histograms are not present in the background and correspond to the  $^{238}\text{U}$  and  $^{232}\text{Th}$ , respectively.

The gates restrict allowed energy values from one axis and project the allowed counts onto the other, producing 1-D histograms that only show events that come in coincidence with the energy gate of the other detector. Figures 7 and 8 are 1-D projections of the 609-keV  $^{238}\text{U}$  energy gate. We are able to identify some of the gamma rays from  $^{214}\text{Po}$ , a product of the decay chain of  $^{238}\text{U}$ , and in comparison to the histograms in a study by Tillett *et al.*<sup>7</sup> The corresponding energy values are comparable to the transition energies from higher to the first excited state of  $^{214}\text{Po}$ . Lower energies are unable to be distinguished from Compton scattered gamma rays, as they overlap at the same energies and have weak transition probabilities of only 5% and 3%.

Figures 9 and 10 are 1-D projections of the 2614 keV energy gate that corresponds to  $^{232}\text{Th}$ . The relative intensity and shape of the peaks are comparable to the the histograms in the study by Tillett *et al.*<sup>7</sup> for  $^{232}\text{Th}$ , and the measured values also yield the transition energy values from higher states to the first excited state of  $^{208}\text{Pb}$ .

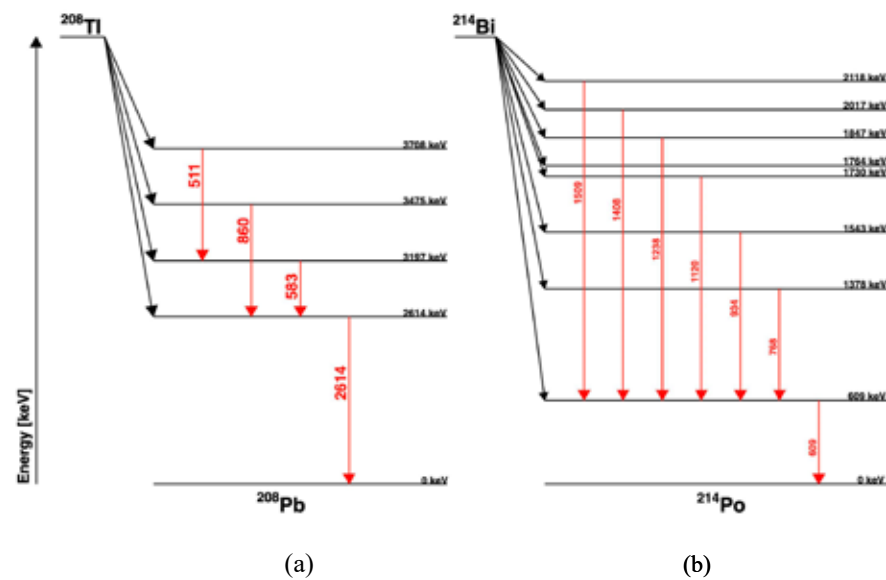


FIGURE 4:  $^{208}\text{Tl}$  to  $^{208}\text{Pb}$  (a) and  $^{214}\text{Bi}$  to  $^{214}\text{Po}$  (b) transitions show the origination of expected gamma energies from the parent nuclei  $^{232}\text{Th}$  and  $^{238}\text{U}$ .

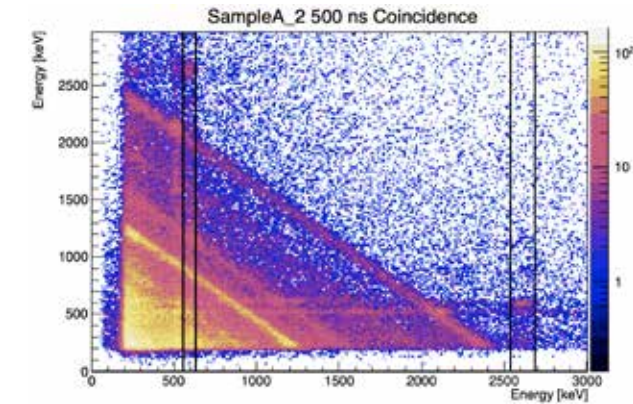


FIGURE 5: Sample A 2-D coincidence histogram with coincidence gates of  $^{238}\text{U}$  (609 keV) and  $^{232}\text{Th}$  (2614 keV), shown by vertical black lines.

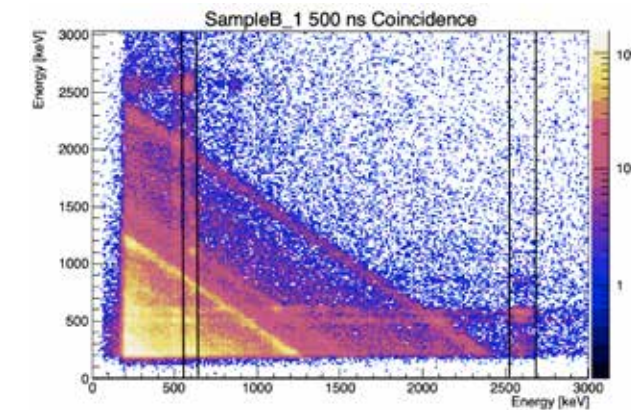


FIGURE 6: Sample B 2-D coincidence histogram with coincidence gates of  $^{238}\text{U}$  (609 keV) and  $^{232}\text{Th}$  (2614 keV), shown by vertical black lines.

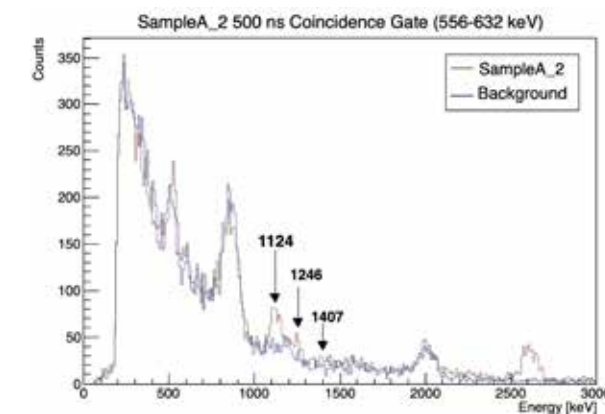


FIGURE 7. Sample A 1-D projection to Y-axis of the  $^{238}\text{U}$  (609 keV) coincidence gate. The labeled peaks correspond to transitions from Fig. 4 ( $^{214}\text{Po}$ ).

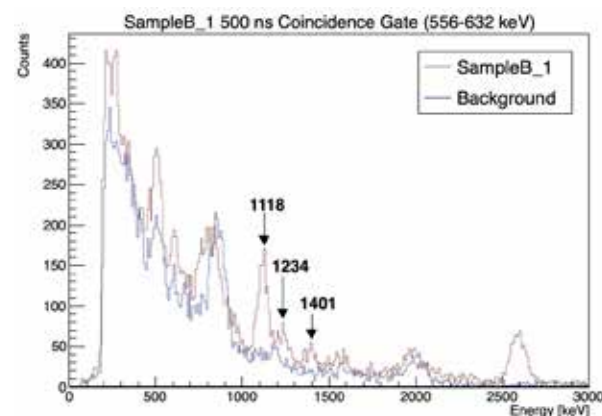


FIGURE 8. Sample B 1-D projection to Y-axis of the  $^{238}\text{U}$  (609 keV) coincidence gate. The labeled peaks correspond to transitions from Fig. 4 ( $^{214}\text{Po}$ ).

## CONCLUSIONS

The 1-D histograms produced by the energy coincidence gate method allowed us to crossreference with known transition energies of gamma rays emitted by nuclei in the decay chains of  $^{232}\text{Th}$  and  $^{238}\text{U}$  to determine the present radionuclides.

Upon confirming the presence of  $^{232}\text{Th}$  and  $^{238}\text{U}$ , next steps include improving our understanding of our detector efficiencies so that we can quantify the activities of the radionuclides in the soil samples. Additionally, we would also need accurate measurements of the masses of the samples without the bottle.

The measured peaks from the 1-D gated coincidence plots for sample B have more counts than sample A. As the run times for both samples are the same, this variance can point to a difference in activity of the radionuclides. The study by Mubarak et al. collected 12 samples with a spacing of 600 m between each on the Nile Delta.<sup>1</sup> Future plans include mapping out a larger region for bigger sample size and showing if there is variation in the concentration of monazite near the Mississippi River.

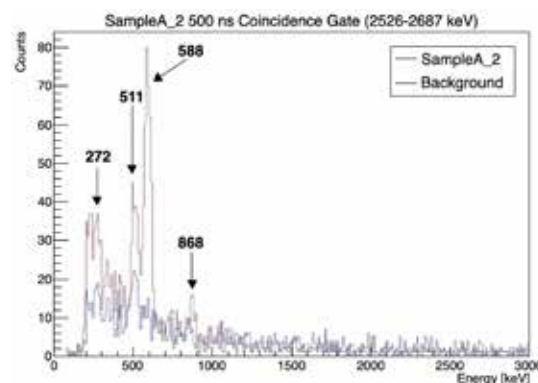


FIGURE 9: Sample A 1-D projection to Y-axis of the  $^{232}\text{Th}$  (2614 keV) coincidence gate. The labeled peaks correspond to transitions from Fig. 4 ( $^{208}\text{Pb}$ ).

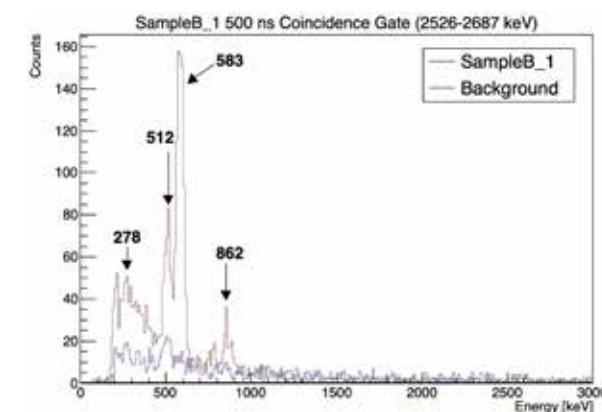


FIGURE 10: Sample B 1-D projection to Y-axis of the  $^{232}\text{Th}$  (2614 keV) coincidence gate. The labeled peaks correspond to transitions from Fig. 4 ( $^{208}\text{Pb}$ ).

## ACKNOWLEDGMENTS

We would like to thank Keith Frye, Adian Edmondson, Ashley Ip, and Sabid Hossain for their contributions to the experimental setup. We would also like to thank Ronald Unz for the collection and preservation of samples from the Great River Road State Park.

## REFERENCES

1. F. Mubarak, M. Fayed-Hassan, N. A. Mansour, T. S. Ahmed, and A. Ali, *Sci. Rep.* **7** (2017).
2. J. Santos, H. Conceicao, M. Leandro, and M. Rosa, *Braz. J. Geol.* **48**, 721–733 (2018).
3. J. Mertie, Jr., “Monazite placers in the Southeastern Atlantic states,” *Geological Survey Bulletin* 1390 (1975).
4. A. Bicker, Jr., “Economic minerals of Mississippi,” *Mississippi Geological Economic and Topographical Survey* (1970).
5. V. Vineethkumar, R. Akhil, K. P. Shimod, and V. Prakash, *J. Radioanal. Nucl. Chem.* **327**, 1–10 (2021).
6. Rene Brun and Fons Rademakers, *Proceedings AIHENP’96 Workshop, Lausanne, Sept. 1996*.
7. A. Tillett, L. Benninger, J. Dermigny, and C. Iliadis, *Appl. Radiat. Isot.* **141**, 24–32 (2018).
8. A. Tillett, J. Dermigny, M. Emamian, Y. Tonin, I. Bucay, R. L. Smith, M. Darken, C. Dearing, M. Orbon, and C. Iliadis, *Nucl. Instrum. Methods Phys. Res., Sect. A* **871**, 66–71 (2017).

### Plenary speakers



Julianne Pollard-Larkin  
MD Anderson Cancer Center



K. Renee Horton  
NASA



Rush Holt Jr.  
former CEO of AAAS



Sarah Hörst  
Johns Hopkins University

### Special Centennial Speakers

Eric Cornell | Jim Gates | Jocelyn Bell-Burnell | John Mather

[www.sigmapisigma.org/congress/2022](http://www.sigmapisigma.org/congress/2022)



phys  
con  
2022 Physics Congress

# Development of an Optical Tweezers Demonstration

Eric Youngsang Ji<sup>a)</sup> and Trey Holik III<sup>b)</sup>

Angelo State University, 2601 W Ave. N, San Angelo, Texas 76909, USA

<sup>a)</sup>Corresponding author: [youngsang1026@gmail.com](mailto:youngsang1026@gmail.com)

<sup>b)</sup>[eddie.holik@angelo.edu](mailto:eddie.holik@angelo.edu)

**Abstract.** Optical tweezers are important tools that are used in several scientific fields. An optical tweezers demonstration was developed by testing several different lasers, particles, and particle environments. The final product was a semienclosed 3D-printed casing with a sooted base plate. This demonstration picked up soot particles using a 250-mW 650-nm laser coupled to a 29-mm diopter focusing lens by Edmund Optics [1].

## INTRODUCTION

Optical tweezers are important tools that use a converging laser beam to trap particles at the beam's focal point. To promote STEM and, more specifically, laser physics, an optical tweezers demonstration kit for Society of Physics Students (SPS) outreach events has been developed.

The goals of the development project were as follows:

- **Safe.** As the minimum hold power required for an optical tweezers laser is 24 mW [1] and the lasers used for this project were 200 mW (for a 650-nm beam), safe handling of the beam and a beam dump were needed. Also, trapped particles are nanosized and can become an irritant as an aerosol. An enclosed container or special environment for the particles was needed.
- **Inexpensive.** Most optical tweezer experiments are \$2000–\$5000 [2], but when used only for demonstrations, a high-grade experiment kit is not needed. Creating a kit for less than \$100 that includes optics by Edmund Optics [3] was desired.
- **Easy, consistent, and repeatable.** The objective of this demonstration was to show that particles were being trapped and followed the laser's focal point. We needed a high rate of successful trapping of the particles.
- **Easy to understand.** Practical and accessible explanation materials were needed. For this demonstration, we used optical simulations with conservation of momentum in GeoGebra [4].

To achieve these goals, we tested different kinds of particles, different lasers and coupled lenses, and different positioning (to find the perfect focal point). We also looked at different visual learning materials to help students understand the theory behind optical tweezers. The most recent iteration of our demonstration and our project files can be seen and recreated on Project Evolution in a GitHub repository [5].

## Optical Tweezers Theory

The basic theory behind optical tweezers can be explained with conservation of momentum. When the ray of a beam is incident on a dielectric particle, it refracts inside the particle [6] as in Fig. 1(a). As the direction of the ray changes due to refraction, the momentum of the ray also changes. Due to the conservation of momentum, radiant pressure at the surface of the particle, shown as  $p_a$  and  $p_b$  in Fig. 1(a), is applied. The total pressure,  $\vec{p}_1$ , applied to the particle causes an acceleration toward the center of the beam. When using a TEM-00 mode beam, the ray in the center of the beam is strongest and it is cylindrically or azimuthally symmetric around the axis of the beam at  $CO$ . The restoring force,  $\vec{p}_1$ , causes the particle to stay in the axis of the beam as in Fig. 1(b). However, the rays of the

beam will keep accelerating the particle in the direction of the beam, so a parallel beam is not suitable for optical tweezers [4].

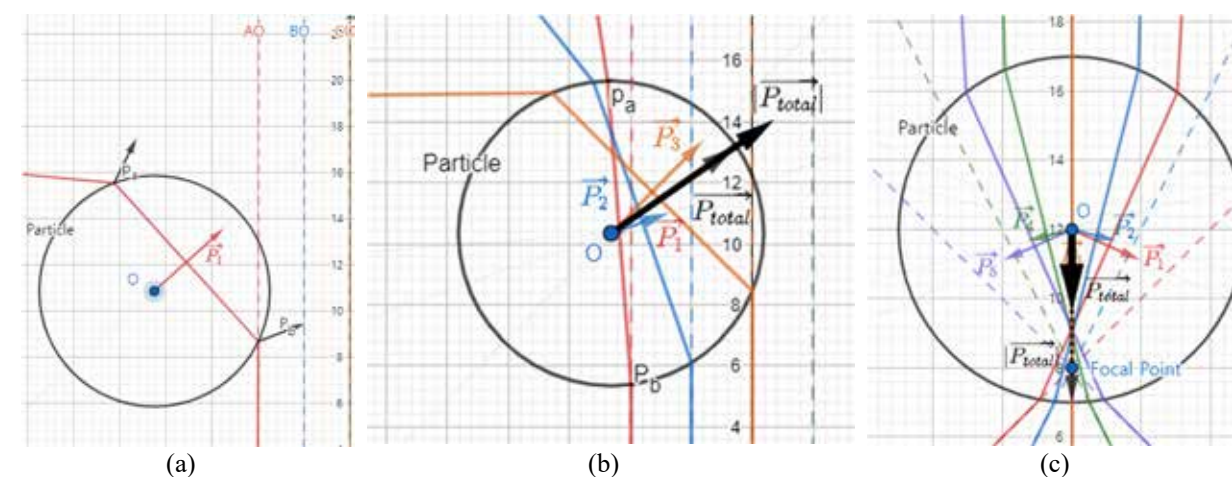


**FIGURE 1.** GeoGebra simulation with parallel rays (the beam direction is up) and a particle. (a) When the particle is incident with the outer rays of the beam, the rays are refracted. This results in a change of momentum at the first and second refraction, shown as  $p_a$  and  $p_b$ , respectively, and a net force shown as  $\vec{p}_1$ . (b) When the particle is inside the beam, the applied net force on the particle is shown as  $\vec{p}_{total}$ . Its unit vector, with a length of the radius of the particle, is  $|\vec{p}_{total}|$ . (c) When the particle is beyond the focal point of the beam, there is some range where the direction of the net force applied to the particle is against the direction of the beam.

As shown in the images of Fig. 1, any displacement from the center of the laser beam will result in a restoring force back to equilibrium. Any particle within the restoring range of the beam is trapped at the equilibrium point, where the focal point is.

## DEMONSTRATION

To begin the demonstration, the theory behind optical tweezers is explained. We used the GeoGebra optical tweezers simulation to show that particles in a parallel beam feel pressure to move toward the beam axis, and the particles in the focused beam stay at the focal point.

Then the physical demonstration starts. Five designs were tested and can be found in the GitHub repository [5]. This paper introduces the latest design, with improved designs located in the GitHub repository. A nominally 250-mW, 650-nm, class-III B laser was used, and all safety guidelines from the Occupational Safety and Health Administration [7] were followed. As the beam was focused with a high focal angle, rays beyond 5 cm from the focal point were weak enough to be considered safe. The particles came from soot on a glass cover slip; however, any surface where soot can be placed works. A lens with a diameter of 9 mm and focal length of 27 mm was used. The rail for the laser and the lens was 3D printed as one piece to secure both the lens and the laser, as shown in Fig. 2(b), and to ensure safety by inhibiting a concentrated reflected beam. The sooted glass was secured with a 3D-printed container as shown in Fig. 2(a).

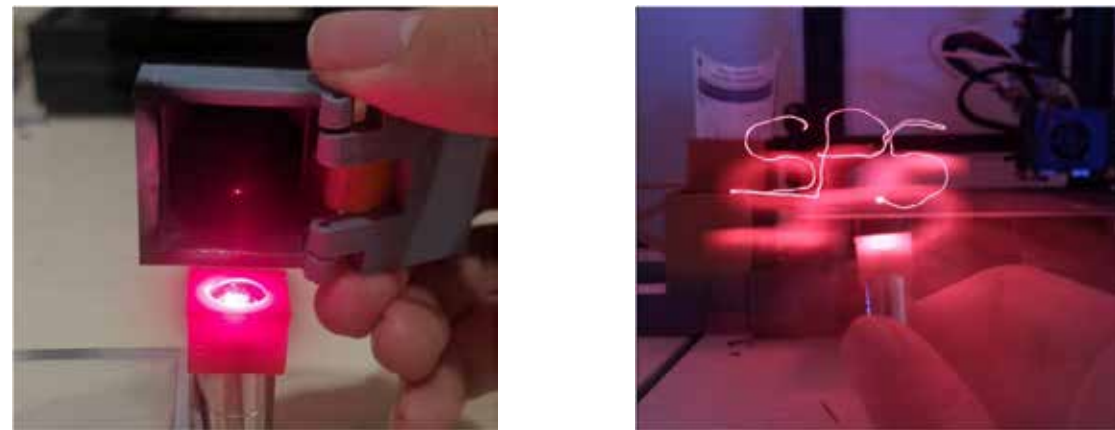
We start with the sooted glass container close to the laser aperture, as shown in Fig. 2(b). Slowly we move the sooted container away from the laser and pass the sooted surface through the focal point. As the sooted glass passes through the particle trapping zone, an  $\sim 1.5\text{-}\mu\text{m}$  soot particle is removed and trapped as shown in Fig. 3(a). When properly focused, the laser was strong enough to trap the particles in air, and we could move the laser without dropping the particles. We demonstrated the strength of the particle tweezers by writing “SPS” in the air with a long exposure camera, as shown in Fig. 3(b). The associated videos in the GitHub repository show the actual demonstration [5].



(a)

(b)

**FIGURE 2.** Diagram of the setup: (a) 3D-printed container with a sooted glass plate inside, and (b) particle being removed from the sooted surface. See GitHub repository for improved designs.



(a)

(b)

**FIGURE 3.** (a) Trapped particle. (b) The particle was moved/accelerated to spell “SPS” during a long exposure image.

## CONCLUSION

With this project we introduced the theory behind optical tweezers using GeoGebra simulations and created a demonstration kit for less than \$100, meeting our initial goals. In the future we will write a detailed manual that SPS chapters at other schools can use to create optical tweezers and demonstrate this phenomenon.

## ACKNOWLEDGMENTS

I am grateful to David Bixler for providing feedback and design ideas, Michael Holcomb and Kenneth Carrell for reviewing and providing feedback on the demonstration, and Jody Casares for providing 20×20 mm glass cover slips and other materials that were used in this project.

## REFERENCES

1. D. Smalley, E. Nygaard, K. Squire, J. Van Wagoner, J. Rasmussen, S. Gneiting, K. Qaderi, J. Goodsell, W. Rogers, M. Lindsey, K. Costner, A. Monk, M. Pearson, B. Haymore, and J. Peatross, *Nature* **553**, 486–490 (2018).
2. S. P. Smith, S. R. Bhalotra, A. L. Brody, B. L. Brown, E. K. Boyda, and M. Prentiss, *Am. J. Phys.* **67**, 26 (1999).
3. Edmund Optics, 9.0 mm diam × 27.0 mm FL, uncoated, plano-convex lens no. 32-958.
4. GeoGebra demonstration simulation: <https://www.geogebra.org/m/tbhaewtc>.
5. GitHub repository: <https://github.com/Deckill/OpticalTweezerDemo>.
6. A. Ashkin, *Phys. Rev. Lett.* **24**, 156–159 (1970).
7. US Department of Labor, *OSHA Technical Manual (OTM)*, Sec. III, Chap. 6, <https://www.osha.gov/otm/section-3-health-hazards/chapter-6>.



Applications due  
January 15

# SPS SUMMER INTERNSHIPS





The SPS summer internship offers 10-week long positions in:

- Science Policy
- Communication
- Research
- Education
- Outreach



All internships include paid housing, a competitive stipend, a commuting allowance, and transportation to and from Washington, DC.

For more information and to view the previous work and journal entries of SPS interns, please visit [spsnational.org/programs/internships](https://spsnational.org/programs/internships).

# Dielectric Properties of Nanostructured ZnO Using Impedance Spectroscopy

Grant Mayberry<sup>a)</sup> and Parameswar Hari<sup>b)</sup>

Department of Physics and Engineering Physics, University of Tulsa, Tulsa, Oklahoma 74104, USA

<sup>a)</sup> Corresponding author: [gmm2929@utulsa.edu](mailto:gmm2929@utulsa.edu)

<sup>b)</sup> [parameswar-harikumar@utulsa.edu](mailto:parameswar-harikumar@utulsa.edu)

**Abstract.** This study focuses on the dielectric properties of 21.9-nm spherical zinc oxide (ZnO) nanoparticles (NPs) at room temperature, as a dry powder and suspended in a liquid. Impedance spectra in the frequency range of 100 Hz to 5.1 MHz were used to investigate the frequency-dependent dielectric properties of ZnO NPs. The commercially available ZnO NPs used in this study were suspended in variable volume fractions up to ~1% in deionized (DI) water and unrefined organic coconut oil and subjected to three sonication conditions: no sonication (NS), 1 hour of bath sonication (BS), and 1 hour of bath sonication followed by probe sonication throughout the experiment (CS, “concurrent sonication”) to determine sonication dependence. Small volumes of the resulting suspension were injected sequentially into a dielectric cell for measuring frequency response. Dry particle tests were conducted similarly. Impedance data suggests that the dielectric behavior of ZnO NPs in a liquid suspension is highly dependent on sonication before and during the test and exhibited a strong dependence of dipole with the polarity of the liquid at low frequencies. In addition, a higher dielectric constant of ZnO NPs was observed when the nanoparticles were in suspension than as a dry powder. For frequencies between 100 Hz and 100 kHz, the average dielectric constant of ZnO NPs in DI water, in unrefined coconut oil, and as a dry particle are 368.63, 24.43, and 7.25, respectively.

## INTRODUCTION

Nanostructured ZnO has been investigated as an n-type semiconductor material for third-generation photovoltaics. Nanostructured materials have properties that vary wildly and chaotically with size and morphology, often varying greatly from their bulk counterparts [1]. The properties of bulk materials are independent of size. However, there exists some lower limit of this independence. After this point, entirely new properties can be observed from existing materials structured in new ways. Photovoltaics with nanostructured semiconductor materials such as ZnO NPs are much cheaper and cleaner in their construction than silicon-based photovoltaics, but they do not yet offer the high efficiency of silicon-based photovoltaics [2]. Understanding the dielectric and optical properties of nanomaterials is very important in order to improve their efficiency in photovoltaics. Furthermore, the dielectric properties of any material are important for understanding its behavior in solid-state devices and junctions. Although the experiments outlined in this study cover frequencies well below meaningful optical frequencies, the methodology could be extended to higher frequencies to determine the frequency-dependent complex index of refraction for various nonmagnetic nanomaterials. In this study the dielectric constant of suspended particles is determined by the following relation, derived from Ref. [3] (see Appendix A for full derivation):

$$\epsilon_s^* = \epsilon_e^*(\epsilon_r^* - 1)\phi + \epsilon_e^* \quad (1)$$

where  $\epsilon_s^*$  is the complex dielectric constant of a suspension of spherical NPs,  $\epsilon_e^*$  is the complex dielectric constant of the suspension media,  $\phi$  is the volume fraction of NPs in suspension, and  $\epsilon_r^*$  is the complex dielectric constant of the NPs.

## APPARATUS AND METHODOLOGY

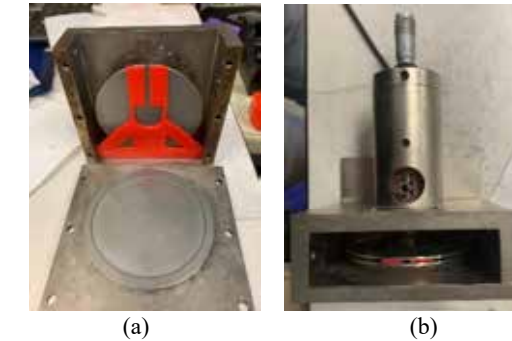


**FIGURE 1.** The apparatus used in this study is shown (a) open to reveal the custom 3D-printed model and (b) ready for use. This dielectric cell was constructed from a 2-mm-wide custom 3D-printed PLA (polylactic acid) model, sanded flat, and placed in an IET Labs LD-3 rigid dielectric cell. Kelvin probes were attached to both leads, leading to a Zurich Instruments MFIA impedance analyzer. Liquid samples were injected and solid samples funneled through the long neck at the top of the 3D model. The 3D model was printed with 100% infill and exhibited no permanent deformation throughout the study.

The apparatus shown in Fig. 1 is the product of an iterative process we used to find the ideal equipment to determine the dielectric properties of a small volume of powder. Samples are prepared by measuring out a few tenths of a gram of ZnO NPs into 3 mL of liquid. The resulting suspension is sonicated for an hour to produce a homogenous stock. This is diluted over various amounts into more suspension media and allowed to settle before being subjected to various sonication conditions, and the dielectric constant of each is determined. This is done to produce a curve of dielectric constant vs volume fraction of NPs for each frequency, sonication condition, and suspension media. Each test consisted of injecting 25  $\mu$ L of test suspension (or ~0.02–0.05 g of powder) and taking impedance spectra from 100 Hz to 5.1 MHz with a test voltage of 300 mV. Ten injections are performed in each test, totaling 250  $\mu$ L of test suspension in the dielectric cell (or around 0.1 g of powder). By the methods outlined in Ref. [4] and Appendix B,  $\epsilon_r^*$  can be determined across all frequencies for any suspended or dry powder from these spectra. This methodology was conducted four times each for ZnO NPs in DI water and three times in coconut oil after no sonication (NS), 1 hour of bath sonication (BS), and 1 hour of bath sonication followed by probe sonication throughout the experiment (CS, “concurrent sonication”), totaling 21 experiments and 210 spectra. In addition, 9 CS coconut oil suspensions were tested (90 spectra), and 14 volumes of powder were tested (14 spectra).

## RESULTS

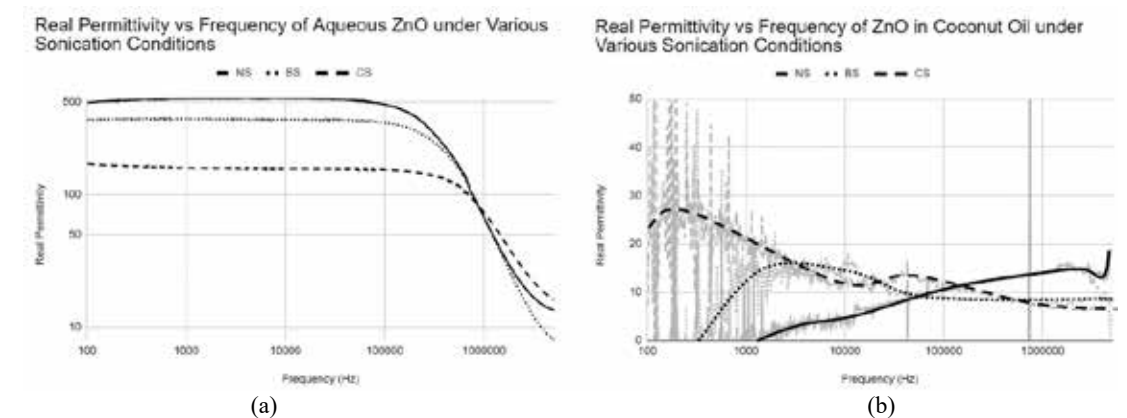


**FIGURE 2.** The sonication dependence of the real component of the dielectric spectra of ZnO NPs in (a) DI water and (b) coconut oil. The noisy appearance of the dielectric spectra in coconut oil can be attributed to the high resistivity of coconut oil. The solid dotted and dashed lines represent the dielectric constants for ZnO NP suspensions subjected to NS, BS, and CS, respectively.

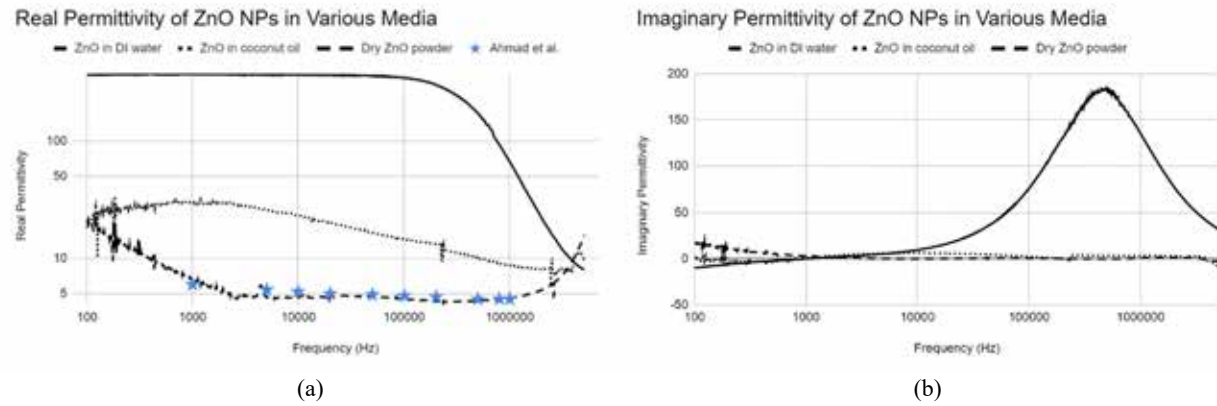


**FIGURE 3.** The (a) real and (b) imaginary components of the dielectric constant of ZnO NPs suspended in each fluid. The solid, dotted, and dashed lines represent the dielectric properties for ZnO NPs in water subjected to BS, coconut oil subjected to CS, and dry air, respectively. Note that Figs. 2 and 3 do not match up concerning coconut oil. This is because of the additional 9 CS coconut oil experiments included in Fig. 3. Data from previous literature is highlighted as well [5].

The experiments in sonication dependence shown in Fig. 2 show that CS yielded the most repeatable results in coconut oil ( $R^2 \approx 1$  for Eq. (1) for most frequencies). This is not the same for DI water, possibly due to the physically invasive probe sonicator and the solvent and conductive nature of DI water. In any case, BS provided the most reliable results ( $R^2 \approx 1$  for Eq. (1) for most frequencies) in DI water. As shown in Fig. 2, regardless of sonication condition, ZnO NPs exhibit a higher dielectric constant across the spectrum in DI water ( $\delta \approx 2.95$  [6]) than in coconut oil ( $\delta$  very low, nonpolar). This is consistent with Fig. 3. Although 14 dry powder tests were conducted, only 7 were included in Fig. 3, due to the NPs exhibiting charging behavior. When the charged and uncharged data were separated, it was clear the charged particles exhibited a much higher dielectric constant. This data was not included in Fig. 3 to maintain consistency. This charging may also explain the sudden increase in dielectric constant at higher frequencies in dry ZnO NPs; such an increase was not observed in the charged powder dielectric spectra.

## CONCLUSIONS

Figure 2 demonstrates the claim that the dielectric properties of suspended ZnO NPs are highly dependent on sonication, showing the importance of material distribution in dielectrics made of multiple materials. The CS experiments in coconut oil and BS experiments in DI water hold the most meaningful data as large complexes of coalesced particles are continually redistributed, meaning the assumptions made in Eq. (1) are valid. Figure 3 demonstrates that ZnO NPs are a stronger dipole in more polar fluids at low frequencies. The ZnO NPs exhibit a real dielectric component at  $\sim 370$  when suspended in DI water at low frequencies, while only reaching  $\sim 30.7$  over the same range when suspended in coconut oil. As a dry powder, ZnO NPs exhibit dielectric constants in the single digits ( $\epsilon \approx 4-7$ , from 1 kHz to 1 MHz, consistent with previous literature [5]). Across the majority of test frequencies, suspended ZnO NPs exhibited higher dielectric constants than dry powder, shown in Fig. 3.

## ACKNOWLEDGMENTS

We would like to thank the University of Tulsa Department of Physics and Engineering Physics for their facilities, Ganga Neupane for his expertise in the operation of Zurich Instruments, Richard Portman and Rusiri Rathnasekara for their assistance preparing and imaging TEM images, Gabriel LeBlanc for the use of his lab equipment and 3D printing expertise, and the Oklahoma Photovoltaic Research Institute.

## REFERENCES

1. G. Guisbiers, S. Mejía-Rosales, and F. Deepak, *J. Nanomater.*, **2012**, 1 (2012).
2. A. Wibowo, M. Marsudi, M. Amal, M. Ananda, R. Stephanie, H. Ardy, and L. Diguna, *RSC Adv.* **10**, 42838 (2020).
3. C. Grosse and V. Shilov, *J. Colloid Interface Sci.* **309**, 283 (2007).
4. A. Kordzadeh and N. de Zanche, *Concepts Magn. Reson.* **46**, 19 (2016).
5. P. Ahmad, A. Rao, K. Babu, and G. Rao, *Mater. Chem. Phys.* **224**, 79 (2019).
6. A. Gubskaya and P. Kusalik, *J. Chem. Phys.* **117**, 5290 (2002).

# Remarkable Topological Features of Electronic Band Dispersion of IrGa and RhGa Compounds from First Principles

Jean P. Alvarez,<sup>1, a)</sup> David Gordon,<sup>1, b)</sup> Jack Howard,<sup>2, c)</sup> Joshua Steier,<sup>2, d)</sup> Kalani Hettiarachchilage,<sup>3, e)</sup> and Neel Haldolaarachchige<sup>1, f)</sup>

<sup>1)</sup>Department of Physical Science, Bergen Community College, Paramus, New Jersey 07652, USA

<sup>2)</sup>Department of Physics, Seton Hall University, South Orange, New Jersey 07079, USA

<sup>3)</sup>Department of Physics and Astronomy, College of Staten Island, 2800 Victory Blvd., Staten Island, New York 10314, USA

<sup>a)</sup>Corresponding author: [jpa113@rutgers.edu](mailto:jpa113@rutgers.edu)

<sup>b)</sup>[gordo.1025@gmail.com](mailto:gordo.1025@gmail.com)

<sup>c)</sup>[jack.howard@student.shu.edu](mailto:jack.howard@student.shu.edu)

<sup>d)</sup>[joshua.steier@stonybrook.edu](mailto:joshua.steier@stonybrook.edu)

<sup>e)</sup>[kalani.hettiarachchilage@shu.edu](mailto:kalani.hettiarachchilage@shu.edu)

<sup>f)</sup>[nhaldolaarachchige@bergen.edu](mailto:nhaldolaarachchige@bergen.edu)

**Abstract.** Exotic behavior of linearly dispersed electronic bands near the Fermi level implies advanced physical properties in a material. In this paper, we present an *ab initio* study of the electronic properties of *IrGa* and *RhGa*, with and without spin-orbit interaction, using first-principles calculations. Linearly dispersed band crossings, reminiscent of topological semimetallic band structures, were identified near the Fermi energy. These include type-I and type-II Dirac points and nodal lines. By applying compressive and tensile stress to the lattice along x, y, and z, the response to the band structure near the Fermi level has been studied.

## INTRODUCTION

The field of topological matter is currently one of the most active, and hence discovering new exciting topological materials is of interest. Among topological materials, topological insulators and semimetals are classified as topological if nontrivial Chern numbers or Berry phases can be detected. Just as with normal insulating materials, topological insulators have an energy gap between the valence and conduction bands, but they exhibit gapless, conducting states on the surface [1, 2]. Topological semimetals are categorized mainly into three types: Dirac semimetals, Weyl semimetals, and nodal line semimetals. In all these topological semimetals, bands cross in momentum space and are inverted beyond the crossing point (or line) [3]. Weyl and Dirac semimetals exhibit band crossing points, while in nodal line semimetals the bands are degenerate along a 1D nodal line or loop. Nodal line semimetals can be the origin of many different topological phases; spin-orbit coupling can gap to a nodal line, Weyl points, Dirac points, or to a topological insulating phase, depending on the crystal symmetry. For example, to have a Weyl semimetal, either inversion or time-reversal symmetry needs to be broken [4, 5].

Dirac materials have a linear or quasilinear band dispersion (Dirac bands) near the Fermi energy, which is ineffable within the nonrelativistic Schrödinger description but can be described by the Dirac equation by considering massless high-mobility electrons. Such a Dirac band dispersion was first predicted in graphene [6, 7], which exhibits six Dirac points. The linear crossing point at the Fermi level in graphene has been linked to its electronic and optical properties. After the discovery of graphene, the search for Dirac materials was extended to 3D materials [8,9,10]. Dirac semimetal behavior was first predicted and then realized in  $\text{Na}_3\text{Bi}$  and  $\text{Cd}_3\text{As}_2$  [8,14-20,47], Weyl semimetal behavior was predicted and realized in  $\text{TaAs}$  [32, 41-46], and nodal line semimetal behavior was predicted in  $\text{Cu}_3\text{PdN}$ ,  $\text{Ca}_3\text{P}_2$ ,  $\text{CaP}_3$ ,  $\text{PbO}_2$ ,  $\text{CaAg}$ ,  $\text{TiB}_2$ ,  $\text{CaAgAs}$ ,  $\text{ZrB}_2$ ,  $\text{SrSi}_2$ ,  $\text{LaSiS}$  [9,23-31] and experimentally realized in  $\text{PbTaSe}_2$ ,  $\text{PtSn}_4$ ,  $\text{ZrSiS}$ ,  $\text{ZrSiSe}$ ,  $\text{ZrSiTe}$ ,  $\text{HfSiS}$ , and  $\text{ZrSnTe}$  [32-40]. Linear band crossing points can be classified into two categories by considering the slope of the band dispersion at the crossing point. Type-I Dirac points are “upright” in respect to energy, while type-II Dirac points are tilted, thus having unequal slopes of the band dispersions. These two types differ in their density of states at the Fermi level, which vanishes for type-I Dirac nodes but is finite for type-II nodes [11-13]. In general, first-principles electronic structure calculations based on density functional theory (DFT) play an important role in exploring topological electronic materials theoretically.

In this work, a detailed study of the electronic band structure and density of states of iridium gallium (*IrGa*) [53, 54], and rhodium gallium (*RhGa*) is presented and their topological nature is reported. To the best of our knowledge, these compounds have not yet been discussed in detail for their topological behaviors. In this paper, we report

calculated electronic structures of *IrGa* and *RhGa*, and predict that both compounds exhibit topological features. The same features are observed in both compounds; hence we mainly present the detailed study of *IrGa*. In the *IrGa* bulk band structure there are highly dispersive bands that cross the Fermi level. Without the SO effect, a nodal line formed by the highly dispersive bands is located near the Fermi level around the R point. The nodal line is protected in the absence of SO and is gapped due to SO coupling. Along M-R, there is a type-1 Dirac crossing. A flat band can be seen along M-R near the Fermi level that crosses the linear bands twice and gaps out with SO coupling. Additionally, the pressure effect of the material was tested.

## CRYSTAL STRUCTURE AND COMPUTATIONAL METHOD

Electron configurations of *Ir*, *Rh*, and *Ga* are  $[Xe]4f^{14}5d^76s^2$ ,  $[Kr]4d^85s^1$ , and  $[Ar]3d^{10}4s^24p^1$ , respectively. The *Ir(Rh)*-d orbitals and *Rh*-s orbitals are not fully occupied, whereas *Ga*-p orbitals are not fully occupied. Both are intermetallic compounds with a cubic lattice structure. The lattice parameters of *IrGa* and *RhGa* are 3.0040 and 3.0034, respectively, [55] with the same space group symmetry of 221 (Pm-3m). The crystal is symmorphic in that it has both time-reversal and inversion symmetry. The optimized lattice parameter for *IrGa* is calculated by using volume optimization as  $a = 3.0566$  and is used for all the calculations. It is comparable to the reported lattice parameter in Refs. [53,54]. Figure 1 shows the primitive cell structure of *IrGa*, the same as the conventional cell. The *Ga* atoms sit at the corners of the primitive cell, and *Ir (Rh)* atom is at the center of the primitive cell. The first Brillouin zone (BZ) of the structure is shown in the right panel of Fig. 1 with the high symmetry points on the cubic BZ and the  $\Gamma(0, 0, 0)$  point located at the center.

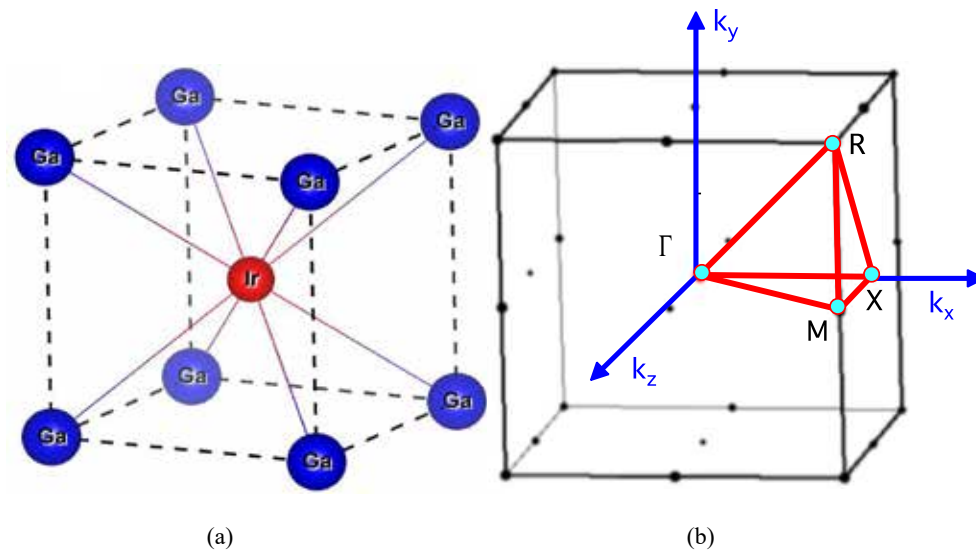


**FIGURE 1.** Structure of bulk *IrGa*. Panel (a): The primitive unit cell. The blue spheres denote the *Ga* atoms and the red sphere is the *Ir* atom. Panel (b): Bulk primitive BZ. The  $k_x$ ,  $k_y$ , and  $k_z$  show the reciprocal lattice vectors. The light blue dots display the high symmetry points of the BZ with labeling  $\Gamma$ , R, X, and M.

The band structure and density of states were calculated by performing first-principles density functional theory (DFT) methods in the WEIN2K simulation package using the Perdew-Burke-Ernzerhof (PBE) pseudopotentials and the plane-wave basis set with the generalized gradient approximation (GGA) [56-60]. The BZ was sampled by using 20,000 k-points and setting the plane-wave cut-off parameters, RKmax, to 7 with extreme convergent of energy and charge. Calculations were performed with and without spin-orbit (SO) coupling. Volume optimization was performed to calculate the lattice parameters to corresponding pressures. The crystal momentum in units of  $k = (\pi/a, \pi/a, \pi/a)$  is used throughout the discussion unless otherwise specified.

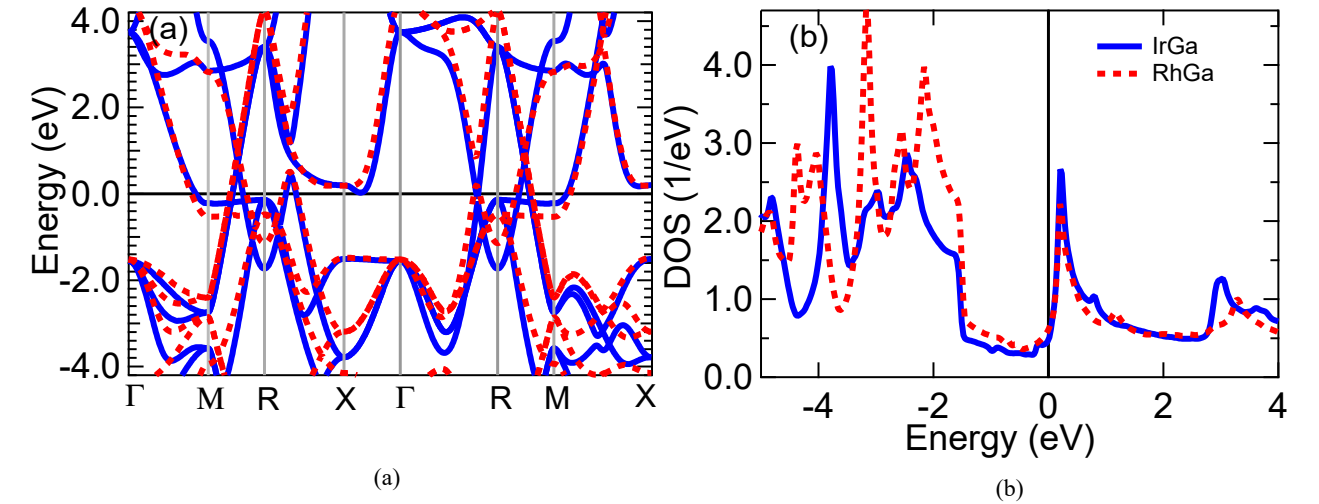


**FIGURE 2.** Calculated electronic band structure and total density of states (DOS) for *IrGa* and *RhGa* compounds without SO coupling. (a): Calculated bulk band structures along the high-symmetry lines on the BZ k-path  $\Gamma$ -M-R-X- $\Gamma$ -R-M-X shown in Fig. 1(b) for *IrGa* (blue solid lines) and *RhGa* (red dotted line). (b): The total DOS of *IrGa* is shown by the blue solid line, whereas the red dotted line shows the total DOS for the *RhGa* compound. The solid black line at zero indicates the Fermi level.

## RESULTS AND DISCUSSION

The band structure calculations of *IrGa* and *RhGa* within GGA without inclusion of the SO coupling along the high-symmetry k-path  $\Gamma$ -M-R-X- $\Gamma$ -R-M-X are plotted by setting the Fermi level to 0 eV on the energy scale, as shown in Fig. 2. The band structures of *IrGa* and *RhGa* are shown in Fig. 2(a) using blue solid lines and red dotted lines, respectively. The features of both band structures are the same. Total DOS calculations for *IrGa* and *RhGa* are shown in Fig. 2(b) by taking the blue solid and red dotted lines discretely. There are no measurable differences in the total DOS either. Due to these similarities, we extend the detailed study by choosing the *IrGa* compound.

The band structures of *IrGa* within GGA without inclusion of the SO coupling along the high-symmetry k-path  $\Gamma$ -M-R-X- $\Gamma$ -R-M-X are plotted in Fig. 3. The left panel (a) shows the band structure of the *IrGa* compound, and the right panel (b) shows the atom-projected DOS calculation. There are few bands near the Fermi level. There is a single band that crosses the Fermi level near point M (shown in the  $\Gamma$ -M and M-X planes), and it was identified as the *Ir*-deg orbital. The range of linearly dispersed bands is large, and linear crossing of bands near the Fermi level is observed and discussed below. The results of the total and atom-projected DOS of *IrGa* help to elaborate on the nature of the bands near the Fermi level and provide information about the origin of the bands and contributions from each atom and each orbital to DOS. According to the results shown in the right panel (b) of Fig. 3, DOS near the Fermi level is very small (essentially a zero DOS at the Fermi level for perfect Dirac semimetals) and is mostly a contribution from the *Ir* atom, which is dominated by d-orbitals, while the contribution from *Ga* is very small. Since the SO couplings can be used to identify exotic band behaviors of Dirac materials, we perform an SO calculation for the *IrGa* system as shown in the bottom part of Fig. 3. The left panel (c) of the figure shows the SO calculation of the band structure which has more degenerated bands and opening gaps corresponding to the absence of SO coupling as discussed below. The right panel (d) of the figure represents the DOS contribution from each atom. When compared to the DOS without inclusion of the SO effect, there is no change in the DOS with SO coupling at the Fermi level, although the DOS near the Fermi surface displays sharp contrast.

Within the chosen k path there are band crossings in the M-R ( $k_x = -\pi/a$ ,  $k_z = -\pi/a$ ) plane near the Fermi level as enumerated from 1-3. Since irreducible representation (symmorphic crystal symmetries) allows us to access each eigenvalue along the chosen k-path, we can see connecting lines of bands and the same colored bands with the same symmetry. A zoomed-in picture of the irreducible representation of the M-R plane is displayed in the left panel of Fig. 4. It is very clear that bin 1 in Fig. 4 is a type-I twofold-degenerate Dirac point located at an energy of about 0.65 eV with the coordinates  $(-0.55342, 0.28948, -0.55342)$ . The linear crossing of the black line (irreducible representations of  $\Gamma_1$  and  $\Gamma_5$  of space group  $C_{4v}$ ) is dominated by hybridized bands of *Ir*-dt<sub>2g</sub> and the *Ga*-s orbital.

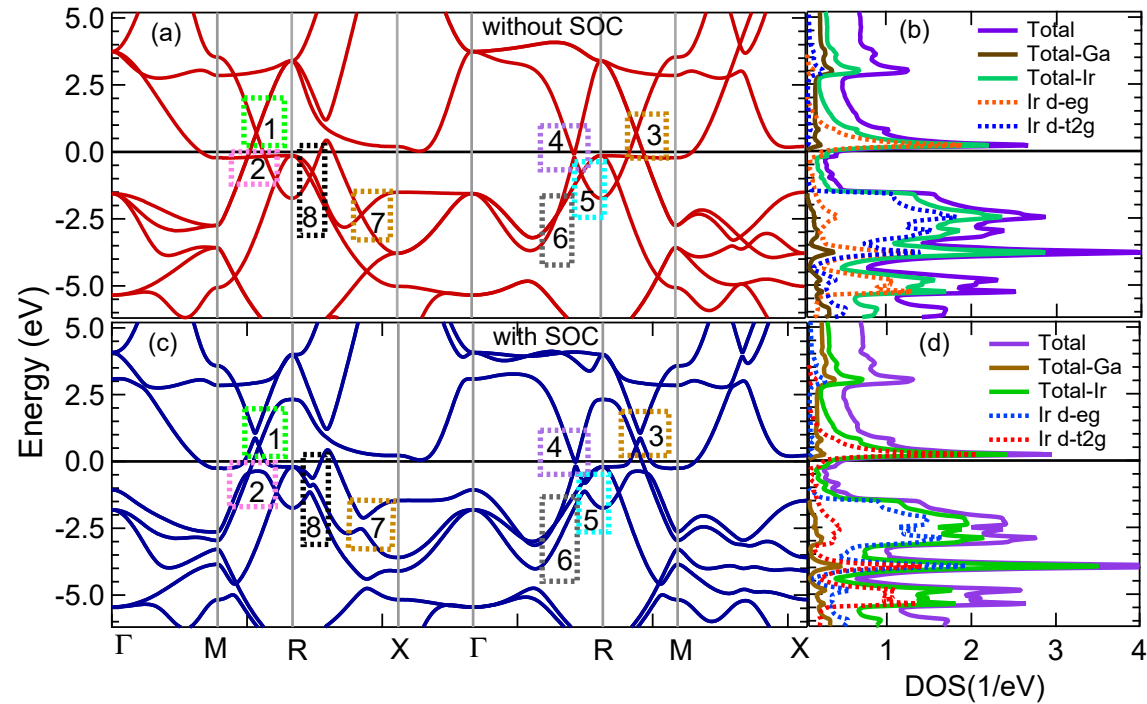


**FIGURE 3.** Calculated electronic band structure and atom-projected DOS for *IrGa* with and without SO coupling (SOC). Panel (a): Calculated bulk band structures along the high-symmetry k-path  $\Gamma$ -M-R-X- $\Gamma$ -R-M-X shown in Fig. 1(b). The numbers from 1 to 8 are discussed in the content. Panel (b): The purple solid line denotes the total density of states of *IrGa*. The maximum contribution to the DOS comes from d orbitals of the *Ir* atoms as shown in the red and blue dotted lines, while *Ga* atoms contribute a small percentage as indicated with the solid brown line. The maximum contribution to the total DOS at the Fermi level forms from deg orbitals of the *Ir* atom. Panel (c): Calculated bulk band structures along the high-symmetry k-path as in the top panel but with SO coupling. Panel (d): The purple solid line denotes the DOS of *IrGa*. The maximum contribution to the DOS comes from d orbitals of the *Ir* atoms as denoted by the red and blue dotted lines, while *Ga* atoms contribute a small percentage as displayed by the solid brown line. The solid black line in all figures at zero indicates the Fermi level.

The gray line ( $\Gamma_5$  of space group  $C_{4v}$ ) is dominated by hybridized bands of *Ir*-dt2g, p, and *Ga*-p orbitals. The black and gray lines at the crossing point display the same and opposite slopes around  $\pm 16$  eV. In the presence of SO coupling, the crossing point is fully gapped into threefold degeneracy with band inversion as shown in the right panel of Fig. 4. In conclusion, the crossing point is predicted to be a Dirac point protected by the absence of SO coupling with a predicted electron velocity of around  $2.4 \times 10^{16}$  /s calculated by  $(1/\hbar)dE/dk$ , which is similar to the experimentally measured velocity of *Cd<sub>3</sub>As<sub>2</sub>* [20]. A flat energy dispersion of electrons at the Fermi level of a material leads to instabilities in the electronic system and can be claimed as a phase transition [63-65]. Within the chosen k path in the M-R plane ( $k_x = -\pi/a$ ,  $k_z = -\pi/a$ ) near the Fermi level, a flat band was predicted in -0.20 eV as enumerated in box 2 in the left panel of Fig. 4 without the SO effect. Although we predict a flat band, there is no singularity present in the DOS as expected to be in a phase transition [65]. With switching on SO coupling, the two crossings at the coordinates  $(-0.55342, 0.29799, -0.55342)$  and  $(-0.55342, 0.34907, -0.55342)$  are gapped out into twofold degeneracy of each as displayed in the right panel of Fig. 4. In irreducible representation the first coordinate consists with  $\Gamma_1, \Gamma_2$ , and  $\Gamma_5$  symmetries and the second coordinate consists with  $\Gamma_1$  and  $\Gamma_2$  that are protected by space group symmetry  $C_{4v}$ . The flat band is identified as *Ir*-deg orbitals. It is observed that the bands are linear and gap out with the SO effect, and the flat band has almost zero slope, while the other bands have around  $\pm 16$  eV. By observation of the tilting of the bands, we predict that to be a type-II nodal line which transitions from a nodal line semimetal to a topological insulator in the presence of the SO effect. Similar single crossing of such a flat band has been discussed in *ScPd<sub>3</sub>* [62].

Additionally, a crossing at the coordinates  $(-0.55342, 0.43422, -0.55342)$  represented by the  $\Gamma_1$  and  $\Gamma_4$  bands with energy -1.0 eV is protected by the  $C_{4v}$  space group symmetry. Bin 3 in the M-R plane represents this crossing, and it opens a small gap (twofold degeneracy) due to the SO effect, which is a nodal line formed around the R point.

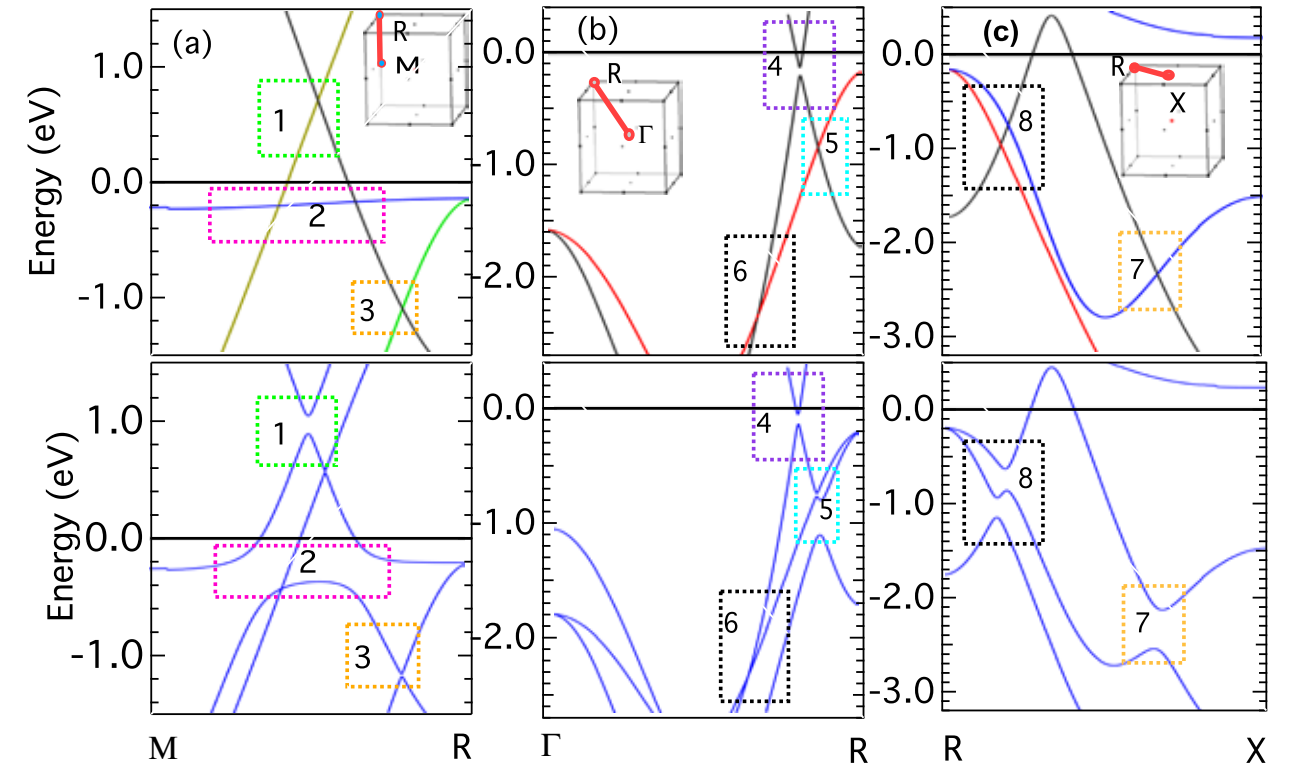


**FIGURE 4.** (Color online) Zoomed-in version of the electronic band structure of bulk *IrGa* in different segments. Panel (a) top: Calculated zoomed-in irreducible band dispersion around areas 1, 2, and 3 in Fig. 3 along the M-R trajectory is presented with the absence of SO coupling. Panel (a) bottom: The same as panel (a) top but with the presence of SO coupling. Panel (b) top: Calculated zoomed-in irreducible band dispersion around 4, 5, and 6 labels in Fig. 3 shown along k-path  $\Gamma$ -R in the absence of SO coupling. Panel (b) bottom: The same as panel (a) top but in the presence of SO coupling. Panel (c) top: Calculated zoomed-in irreducible band dispersion around the 7 and 8 labels in Fig. 3 shown along k-path R-X in the absence of SO coupling. Panel (c) bottom: The same as panel (c) top but in the presence of SO coupling. The insets on panel (a), (b), and, (c) denote the selected M-R,  $\Gamma$ -R, and R-X paths. Zero energy is set to the Fermi level in all panels.

The discussion will be continued in both the M-R-X and  $\Gamma$ -R-X planes and recognized as a three-dimensional nodal line around R related to the labeling boxes 3, 5, and 8 together in Fig. 3, with and without SO coupling.

Moving into the  $\Gamma$ -R trajectory, the zoomed-in picture in Fig. 4 shows that there is an avoided-crossing marked in bin 4. The gap is barely sensitive to the SO effect. The gap with the absence of SO as shown in the top panel of Fig. 4(b) is protected by the  $C_{3v}$  space group and is located at the coordinates  $(-0.43905, 0.43905, 0.43905)$  with band index  $\Gamma_1$ . We freeze the discussion of this feature due to the same symmetries of the bands shown in irreducible representation. Bin 5 in Fig. 4 is related to the end of the nodal line predicted around the R point in  $\Gamma$ -R. A crossing point at the coordinates  $(-0.46948, 0.46948, 0.46948)$  with band indices  $\Gamma_1$  and  $\Gamma_3$  is protected by the absence of the SO effect and falls along the threefold rotation axis with symmetry  $C_{3v}$ . With inclusion the SO gap is opened with threefold degeneracy which is dominated by crossing of *Ga*-s orbitals and *Ir*-deg orbitals. Additionally, bin 6 (-2.2 eV) at coordinates  $(-0.36565, 0.36565, 0.36565)$  in Fig. 4 displays a linear band ( $\Gamma_1$  and  $\Gamma_3$ ) crossing with space group symmetry  $C_{3v}$ , which is protected by inclusion of SO coupling but band index  $\Gamma_1$  is separated.

Box 8 shows a zoomed-in picture of the R-X ( $k_x = k_z$  and  $k_y = \pi/a$ ) plane shown in Fig. 4(c), representing the end of the nodal line located around R. One crossing is located at an energy of -0.95 eV with coordinates  $(-0.46219, 0.55342, -0.46219)$  and band indices  $\Gamma_1$  and  $\Gamma_3$  with the space group symmetry of  $C_{2v}$ . The other crosses at an energy of -0.74 eV with coordinates  $(-0.44395, 0.55342, -0.44395)$  and indices  $\Gamma_1$  and  $\Gamma_3$  of space group symmetry  $C_{2v}$ . They are dominated with *Ga*-s orbitals and *Ir*-deg orbitals and split into three bands with SO included as displayed in Fig. 4(c).

Additionally, a Dirac crossing (mainly from  $Ir-dt2g$  orbitals) indicated in bin 7 at energy -2.33 eV with coordinates  $(-0.18853, 0.55342, -0.18853)$ , and bands indices  $\Gamma_1$  and  $\Gamma_2$  protected by symmetry  $C_{2v}$ , open up the gap with the presence of the SO effect. With the discussion of bins 8-7 together, it is a nodal line protected by the absence of SO effect and transits into a topological insulator state with the band inversion by inclusion of SO coupling.

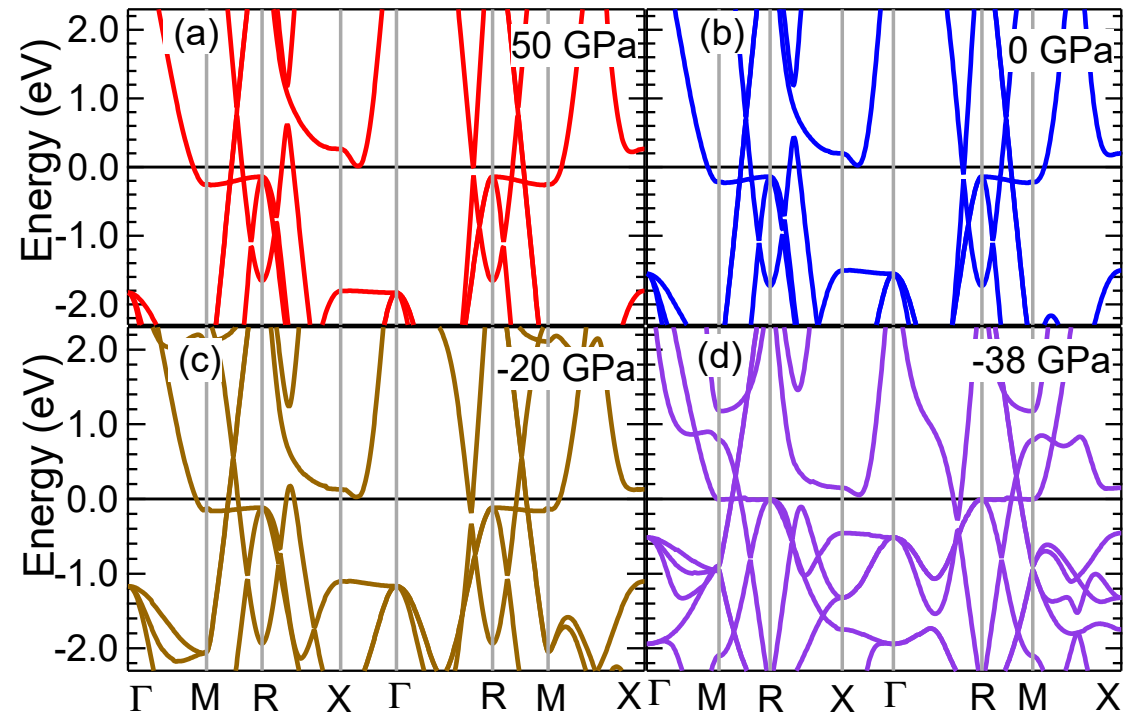


**FIGURE 5.** Band structure of bulk  $IrGa$  under four pressure values. Panel (a): Evolution of bulk band dispersion along high symmetric k-path  $\Gamma$ -M-R-X- $\Gamma$ -R-M-X, the same path used in Fig. 3 for pressure 50 GPa. Panel (b): The same as panel (a) but for pressure 0 GPa. Panel (c): The same as panel (a) but for pressure -20 GPa. Panel (d): The same as panel (a) but for critical pressure -38 GPa.

studies predicted trivial phase transitions into a topological insulator by applying physical pressure [66-69]. To study the topological phases under pressure, volume optimization is performed and the lattice parameter related to applied physical pressure is obtained. The band structure of  $IrGa$  was calculated for both compressive and tensile stress as shown in Fig. 5. The left panel displays the calculated bulk band structure for pressure 50 GPa ( $a = 2.8891$ ), and the top right panel indicates the same for 0 GPa ( $a = 3.0566$ ). There is no impressive effect to the band structure except that the band structure is stretched out more around the Fermi energy. The bottom left panel displays the band structure for -20 GPa ( $a = 3.2006$ ) with the significant differences upon 0 GPa. All the labeling from bins 1-8 have substantial swaps in the energy scale for this particular pressure. Hence, we decide to tune the band structure with tensile stress and originate the critical pressure as -38 GPa ( $a = 3.6594$ ), which brings the flat band in the M-R plane to the Fermi level as shown in the bottom right panel of Fig. 5. A zoomed-in picture of this behavior is displaced in Fig. 6. Figure 6(a) denotes the irreducible representation of band structure in the M-R-X plane for pressure -38 GPa, which shows a closer look of swaps of energy scales due to physical pressure. In this critical pressure, the predicted Dirac point in bin 1 is lowered to 0.3 eV, whereas the flat band is pulled to 0 eV. Although the nodal line around R is broadened out from the Fermi level, in Fig. 6 boxes 7 and 8 band inversion is rendered closer to the Fermi level than they appeared.

Further, there are significant outcomes on total DOS at -38 GPa pressure with SO effect as displayed in Fig. 6(b). It shows that at this critical pressure, both materials will be promising candidates for future studies.

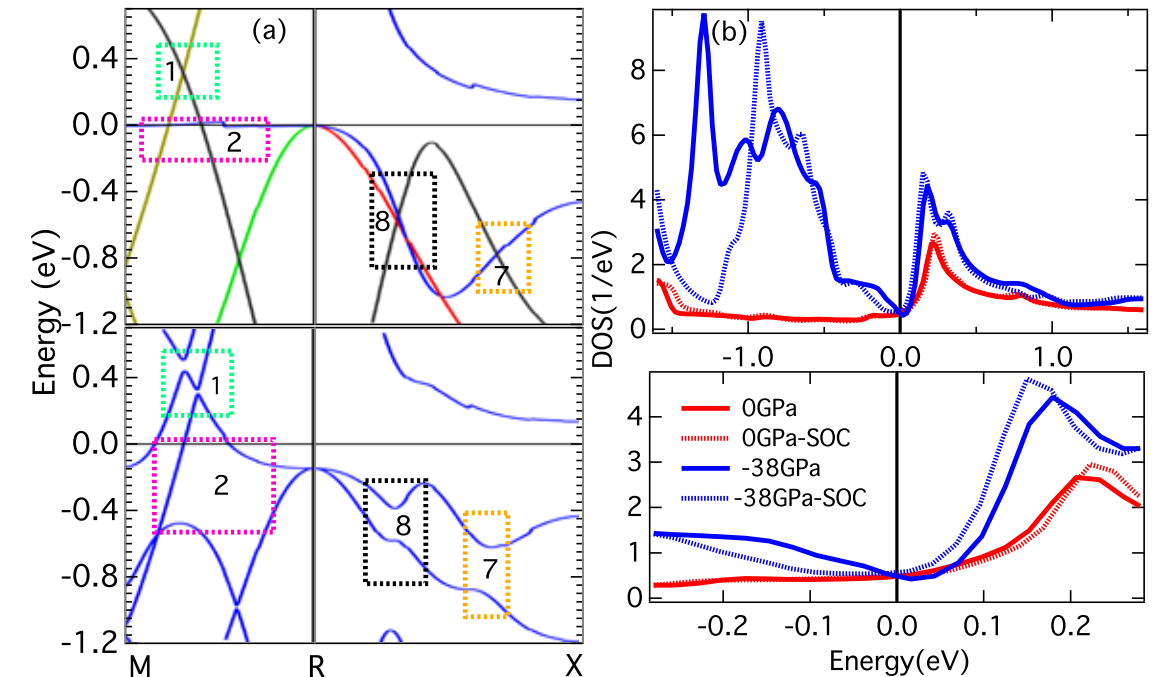


**FIGURE 6.** Zoomed-in version of the bulk band structure in the M-R-X segment with critical pressure -38 GPa and total DOS for critical pressure -38 GPa. Panel (a) top: Calculated zoomed-in irreducible band dispersion in the M-R-X path for bins 1, 2, 7, and 8 in Fig. 3. Panel (a) bottom: The same as panel (a) top but in the presence of SO coupling for pressure -38 GPa. Panel (b) top: Corresponding total DOS of  $IrGa$  for pressure zero and -38 GPa are displayed. The red solid line indicates the total DOS in zero pressure, whereas the blue solid line denotes the same for a critical pressure of -38 GPa. Similarly, the corresponding colored dotted lines show the total DOS for the SO effect for zero and critical pressure, respectively. Panel (b) bottom displays the zoomed-in DOS near the Fermi level. The solid black line at zero indicates the Fermi level.

## CONCLUSION

In summary, our studies of  $IrGa$  and  $RhGa$  compounds suggest that both are important systems to study due to the unusual behavior of bands near the Fermi level and strong spin-orbit coupling effect. Since Dirac material has theoretical and experimental academic significance, further studies of  $IrGa$  and  $RhGa$  are suggested. Most importantly, we predict drastically different topological properties near the Fermi energy with significantly different behaviors of band crossings and touchings. A linear band crossing near the Fermi level was discovered, and Dirac points, nodal lines, and flat bands with tremendously distinct actions were predicted. The SO calculations indicate the degeneracy with band inversions. The predicted unusual electronic structure of  $IrGa$  and its important topological properties will be useful for searching for novel Dirac fermions and materials for further studies.

## ACKNOWLEDGMENTS

D. G., J. P. A., and N. H. acknowledge financial support from a STEMatics grant, Department of Education. N. H. and K. H. acknowledge the Extreme Science and Engineering Discovery Environment (XSEDE), supported by grant number TG-PHY190050.

## REFERENCES

1. M. Z. Hasan and C. L. Kane, *Rev. Mod. Phys.* **82**, 3045 (2010).
2. X. L. Qi, and S. C. Zhang, *Rev. Mod. Phys.* **83**, 1057 (2011).
3. B. J. Yang and N. Nagaosa, *Nat. Commun.* **5**, 4898 (2014)
4. G. Xu, H. Weng, Z. Wang, X. Dai, and Z. Fang, *Phys. Rev. Lett.* **107**, 186806 (2011).
5. A. A. Zyuzin, S. Wu, and A. A. Burkov, *Phys. Rev. B* **85**, 165110 (2012).
6. R. R Nair, P. Blake, A. N. Grigorenko, K. S. Novoselov, T. J. Booth, T. Stauber, N. M. R. Peres, and A. K. Geim, *Science* **320**, 1308–1308 (2008).
7. Y. Zhang, Y. W. Tan, H. L. Stormer, and P. Kim, *Nature*, **438**, 201-202 (2005).
8. Z. K. Liu, J. Jiang, B. Zhou, Z. J. Wang, H. M. Weng, D. Prabhakaran, S-K. Mo, H. Peng, P. Dudin, T. Kim, M. Hoesch, Z. Fang, X. Dai, Z. Shen, D. L. Feng, Z. Hussain, and Y. L. Chen, *Nat. Mater.* **13**, 677-681 (2014).
9. Yu Rui, H. Weng, Z. Fang, X. Dai, and X. Hu, *Phys. Rev. Lett.* **115**, 036087 (2015).
10. S. M. Young, S. Zaheer, J. C. Y. Teo, C. L. Kane, E. J. Mele, and A. M. Rappe, *Phys. Rev. Lett.* **108**, 140405 (2012).
11. H. Huang, S. Zhou, and W. Duan, *Phys. Rev. B* **94**, 121117 (2016).
12. L. Muechler, A. Alexandradinata, Titus Neupert, and R. Car, *Phys. Rev. X* **6**, 041069 (2016).
13. Y. Chen, Y. Xie, S. A. Yang, H. Pan, F. Zhang, M. Cohen, and S. Zhang, *Nano Lett.* **15**, 6974-8 (2015).
14. Z. K. Liu, Y. Zhang, Z. J. Wang, H. M. Weng, D. Prabhakaran, S-K. Mo, Z. X. Shen, Z. Fang, X. Dai, Z. Hussain, and Y. L. Chen, *Science*, **343**, 864-7 (2014).
15. M. Neupane, S-Y. Xu, R. Sankar, N. Alidoust, G. Bian, C. Liu, I. Belopolski, T-R. Chang, H-T. Jeng, H. Lin, A. Bansil, F. Chou, and M. Z. Hasan, *Nat. Commun.* **5**, 3786 (2014).
16. M. Yan, H. Huang, K. Zhang, E. Wang, W. Yao, K. Deng, G. Wan, H. Zhang, M Arita, H. Yang, Z. Sun, H. Yao, Y. Wu, S. Fan, W. Duan, and S. Zhou, *Nat. Commun.* **8**, 257 (2017).
17. H.-J. Noh, J. Jeong, E.-J. Cho, K. Kim, B. I. Min, and B-G. Park, *Phys. Rev. Lett.* **119**, 016401 (2017).
18. Q. D. Gibson, L. M. Schoop, L. Muechler, L. S. Xie, M. Hirschberger, N. P. Ong, R. Car, and R. J. Cava, *Phys. Rev. B* **91**, 205128 (2015).
19. L. M. Schoop, F. Pielnhofer, and B. Lotsch, *Chem. Mater.* **30**, 3155-3176 (2018).
20. T. Liang, Q. Gibon, M. N. Ali, M. Liu, R. J. Cava, and N. P. Ong, *Nat. Mater.* **14**, 280-284 (2015).
21. P. Ho`rava, *Phys. Rev. Lett.* **95**, 016405 (2005).
22. H. Weng, Y. Liang, Q. Xu, R. Yu, Z. Fang, X. Dai, and Y. Kawazoe, *Phys. Rev. B* **92**, 045108 (2015).
23. L. S. Xie, L. M. Schoop, E. M. Seibel, Q. D. Gibson, W. Xie, and R. J. Cava, *APL Mater.*, **3**, 083602 (2015).
24. Q. Xu, R. Yu, Z. Fang, and X. Dai, *Phys. Rev. B* **95**, 045136 (2017).
25. Z. Wang and G. Wang, *Phys. Lett. A* **381**, 2856-2859 (2017).
26. A. Yamakage, Y. Yamakawa, Y. Tanaka, and Y. Okamoto, *J. Phys. Soc. Jpn.* **85**, 013708 (2016).
27. X. Feng, C. Yue, Z. Song, Q. Wu, and B. Win, *Phys. Rev. Mater.* **2**, 014202 (2018).
28. M. Hirayama, R. Okugawa, T. Miyake, and S. Murakami, *Nat. Commun.* **8**, 14022 (2017).
29. G. P. Mikitik and Y. Sharlai, *Phys. Rev. B* **73**, 235112 (2006).
30. H. Huang, J. Liu, D. Vanderbilt, and W. Duan, *Phys. Rev. B* **93**, 201114 (2016).
31. J. Howard, J. Steier, N. Haldolaarchchige, and K. Hettiarachchilage, *J* **4**, 577-588 (2021).
32. S.-M. Huang, S.-Y. Xu, I. Belopolski, C.-C. Lee, G. Chang, B. Wang, N. Alidoust, G. Bian, M. Neupane, C. Zhang, S. Jia, A. Bansil, H. Lin, and M. Z. Hasan, *Nat. Commun.* **6**, 7373 (2015).
33. R. Lou, J.-Z. Ma, Q.-N. Xu, B.-B. Fu, L.-Y. Kong, Y.-G. Shi, P. Richard, H.-M. Weng, Z. Fang, S.-S. Sun, Q. Wang, H.-C. Lei, T. Qian, H. Ding, and S.-C. Wang, *Phys. Rev. B* **93**, 241104 (2016).
34. D. Takane, Z. Wang, S. Souma, K. Nakayama, C. X. Trang, T. Sato, T. Takahashi, and Yoichi Ando, *Phys. Rev. B* **94**, 121108 (2016).
35. Y. Wu, L.-L. Wang, E. Mun, D. D. Johnson, D. Mou, L. Huang, Y. Lee, S. L. Bud'ko, P. C. Canfield, and A. Kaminski, *Nat. Phys* **12**, 667-671 (2016).
36. G. Bian, T-R. Chang, R. Sankar, S.-Y. Xu, H. Zheng, T. Neupert, C.-K. Chiu, S.-M. Huang, G. Chang, I. Belopolski, D. S. Sanchez, M. Neupane, N. Alidoust, C. Liu, B. Wang, C.-C. Lee, H.-T. Jeng, C. Zhang, Z. Yuan, S. Jia, A. Bansil, F. Chou, H. Lin, and M. Z. Hasan, *Nat. Commun.* **7**, 105556 (2016).
37. A. Topp, J. M. Lippmann, A. Varykhalov, V. Duppel, B. V. Lotsch, C. R. Ast, and Leslie M. Schoop, *New J. Phys.* **18**, 125014 (2016).
38. E. Haubold, K. Koepernik, D. Efremov, S. Khim, A. Fedorov, Y. Kushnirenko, J. van den Brink, S. Wurmehl, B. Büchner, T. K. Kim, M. Hoesch, K. Sumida, K. Taguchi, T. Yoshikawa, A. Kimura, T. Okuda, and S. V. Borisenko, *Phys. Rev. B* **95**, 241108(R) (2017).
39. L. M. Schoop, M. N. Ali, C. Straßer, A. Topp, A. Varykhalov, D. Marchenko, V. Duppel, S. S. P. Parkin, B. V. Lotsch, and C. R. Ast, *Nat. Commun.* **7**, 11696 (2016).
40. J. Hu, Z. Tang, J. Liu, X. Liu, Y. Zhu, D. Graf, K. Myhro, S. Tran, C. N. Lau, J. Wei, and Z. Mao, *Phys. Rev. Lett.* **117**, 016602 (2016).
41. S.-Y. Xu, I. Belopolski, N. Alidoust, M. Neupane, G. Bian, C. Zhang, R. Sankar, G. Chang, Z. Yuan, C.-C. Lee, S.-M. Huang, H. Zheng, J. Ma, D. Sanchez, B. Wang, A. Bansil, F. Chou, P. P. Shibayev, H. Lin, S. Jia, and M. Z. Hassan, *Science* **349**, 613-617 (2015).
42. B. Q. Lv, N. Xu, H. M. Weng, J. Z. Ma, P. Richard, X. C. Huang, L. X. Zhao, G. F. Chen, C. E. Matt, F. Bisti, V. N. Strocov, J. Mesot, Z. Fang, X. Dai, T. Qian, M. Shi, and H. Ding, *Nat. Phys.* **11**, 724-727 (2015).
43. A. A. Soluyanov, D. Gresch, Z. Wang, Q. Wu, M. Troyer, X. Dai, and B. A. Bernevig, *Nature* **527**, 495-498 (2015).
44. K. Deng, G. Wan, P. Deng, K. Zhang, S. Ding, E. Wang, M. Yan, H. Huang, H. Zhang, Z. Xu, J. Denlinger, A. Fedorov, H. Yang, W. Duan, H. Yao, Y. Wu, S. Fan, H. Zhang, X. Chen, and S. Zhou, *Nat. Phys.* **12**, 1105-1110 (2016).
45. N. Xu, H. M. Weng, B. Q. Lv, C. E. Matt, J. Park, F. Bisti, V. N. Strocov, D. Gawryluk, E. Pomjakushina, K. Conder, N. C. Plumb, M. Radovic, G. Autès, O. V. Zayzev, Z. Fang, X. Dai, T. Qian, J. Mesot, H. Ding, and M. Shi, *Nat. Commun.* **7**, 11006 (2016).
46. L. Yang, Z. Liu, Y. Sun, H. Peng, H. Yang, T. Zhang, B. Zhou, Yi.Zhang, Y. Guo, M. Rahn, D. Prabhakaran, Z. Hussain, S.-K. Mo, C. Felser, B. Yan, and Y. Chen, *Nat. Phys.* **11**, 728-732 (2015).
47. T.-R. Chang, S.-Y. Xu, D. S. Sanchez, W.-F. Tsai, S.-M. Huang, G. Chang, C.-H. Hsu, G. Bian, I. Belopolski, Z.-M. Yu, S. A. Yang, T. Neupert, H.-T. Jeng, H. Lin, and M. Z. Hasan, *Phys. Rev. Lett.* **119**, 026404 (2017).
48. G. B. Halász and L. Balents, *Phys. Rev. B* **85**, 035103 (2012).
49. P. Hohenberg and W. Kohn, *Phys. Rev.* **136**, B864 (1964).
50. W. Kohn and L. J. Sham, *Phys. Rev.* **140**, A1133 (1965).
51. C. Kittel, *Introduction to Solid State Physics*, 8th ed. (John Wiley & Sons, NY, 2004), pp. 1-704.
52. G. F. Koster, J. D. Dimmock, R. G. Wheeler, and H. Statz, *Properties of the Thirty-Two Point Groups*, 1st ed. (MIT Press, Cambridge, MA, 1963), pp. 1-104.53.
53. K. J. Schulz, O. A. Musbah, and Y. A. Chang, et al., *Bull. Alloy Phase Diagrams* **11**, No. 3, 211-215 (1990).
54. N. Arikani, Z. Charifi, H. Baaziz, H. Unver, and G. Ugar, *Phys. Chem. Solids* **77**, 126-132 (2015).
55. K. J. Schulz, O. Musbah, and Y. Chang, *J. Phase Equilib.* **12**, 10-14 (1991).
56. P. Blaha, K. Schwarz, P. Sorantin, and S. B. Trickey, *Commput. Phys. Commun.* **59**, 399–68. (1990).
57. P. Blaha, K. Schwarz, F. Tran, R. Laskowski, G. K. H. Madsen, and L. D. Marks, *J. Chem. Phys.* **152**, 074101 (2020).
58. J. P. Perdew, K. Burke, and M. Ernzerhof, *Phys. Rev. Lett.* **77**, 3865 (1996).
59. D. J. Singh, et al., *Planewaves, Pseudopotentials, and the LAPW Method*, 2nd ed. (Springer, New York, 1996).
60. G. K. H. Madsen, P. Blaha, K. Schwarz, E. Sjostedt, and L. Nordstrom, *Phys. Rev. B* **64**, 195134 (2001).
61. A. A. Burkov, M. D. Hook, and Leon Balents, *Phys. Rev. B* **84**, 235126 (2011).
62. A. S. Cuamba, H.-Y. Lu, L. Hao, and C. S. Ting, preprint arXiv:1801.01113 [cond-mat.mtrlsci] (2018).
63. N. B. Kopnin, T. T. Heikkila, and G. E. Volovik, *Phys. Rev. B* **83**, 220503 (2011).
64. D. Leykam, A. Andreanov, and S. Flach, *Adv. Phys.: X* **3**, 1473052 (2018).
65. N. Ehlen, M. Hell, G. Marini, E. H. Hasdeo, R. Saito, Y. Falke, M. O. Goerbig, G. Di Santo, L. Petaccia, G. Profeta, and A. Grüneis, *ACS Nano* **14**, 1055-1069 (2020).
66. M. S. Bahrany, P. D. C. King, A. de la Torre, J. Chang, M. Shi, L. Pathey, G. Balakrishnan, Ph. Hofmann, R. Arita, N. Nagaosa, and F. Baumberger, *Nat. Commun.* **3**, 679 (2012).
67. M. S. Bahrany, B.-J. Yang, R. Arita, and N. Nagaosa, *Nat. Commun.* **3**, 679 (2012).
68. M. Hirayama, R. Okugawa, S. Ishibashi, S. Murakami, and T. Miyake, *Phys. Rev. Lett.* **114**, 206401 (2015).
69. H. Gao and W. Ren, *Carbon* **158**, 210-215 (2020).

# Preparing a Manuscript for Publication

Brad Conrad,<sup>1, a)</sup> Rexford Adelberger,<sup>2</sup> and Will Slaton<sup>3, b)</sup>

<sup>1</sup>*Society of Physics Students, American Institute of Physics (AIP), College Park, MD 20782, USA*

<sup>2</sup>*Department of Physics, Guilford College, Greenboro, NC 27410, USA (formerly)*

<sup>3</sup>*Department of Physics and Astronomy, University of Central Arkanas, Conway, AR 72035, USA*

<sup>a)</sup>*Corresponding author: bconrad@aip.org*

<sup>b)</sup>*wvslaton@uca.edu*

**Abstract.** Scientific manuscripts are documents that focus on providing a scientific argument to a specific group. In fact, audience selection is potentially the most important decision a science communicator needs to make before preparing a manuscript for publication. This document will outline a process to draft a manuscript for the *Journal of Undergraduate Reports in Physics* (JURP), but can also be used for most publications. In this specific case, junior or senior physics majors and undergraduate professors are your primary audiences. They are knowledgeable about physics, but unlike you, they have not spent much time trying to understand the specific problem being discussed in your report.

## OVERVIEW

Scientific manuscripts are documents that focus on providing a scientific argument to a specific group. In fact, audience selection is potentially the most important decision a science communicator needs to make before preparing a manuscript for publication. This document will outline a process to draft a manuscript for the *Journal of Undergraduate Reports in Physics* (JURP), but can also be used for most publications. In this specific case, junior or senior physics majors and undergraduate professors are your primary audiences. They are knowledgeable about physics, but unlike you, they have not spent much time trying to understand the specific problem being discussed in your report.

There is a big difference between the comments you write in the margin of your lab notebook and what you might write in a paper for publication in a scientific journal. Your laboratory data book is a chronological, definitive record of everything that you did. It contains all the data, what you did even if it was ultimately wrong, as well as comments as to what you were thinking at that time. A journal article is a focused summary discussion of the research question, its processes, and conclusions. Authors should avoid discussing experimental dead ends and present a clear scientific argument. The reader does not have to be able to completely reproduce the work from the journal article. Instead, the reader should be able to understand both the physics and techniques of what was done and the rationale behind why it was done.

The goal of a journal article is to announce a new finding, idea, or process. Abstracts should provide the key result as most readers will only look at titles and abstracts. By using key words and clear abstracts, potential readers locate research of interest. If, after reading an article, a reader then wants to find out the finer details of an experiment or derivation, they can contact the author of the paper for a personal in-depth conversation about the subtleties.

The general style of writing used in a physics journal is different from that of literary works. The narrative of the paper is intended to do three things: 1) present the background necessary for the reader to understand the science being reported in the paper; 2) outline the details and the implications of your work; 3) lead the reader through the work in such a way that they can clearly follow the rationale leading to your conclusions. When finished with your paper, the reader should not have to decide for themselves what you are proposing. The narrative should lead readers through your work in an unambiguous manner, telling them what to see and understand in what you did. Assist the reader with interpretation of the data and calculations. Presenting a clear interpretation of your results is the most important part of the paper.

You should take care to make sure that the material is presented in a concise and logical way. Make sure that your sentences do not have too many dependent clauses. Overly complicated or long sentences make the logic of an argument difficult to follow. You should choose a paragraph structure that focuses the attention of the reader on the development of the ideas. Paragraphs should connect to each other, as the manuscript is a focused logical argument.

## SECTIONS

### Abstract

An abstract is a self-contained paragraph that concisely explains what you did and presents key results. The abstract is often published separately from the body of the paper, so you cannot assume that the reader of the abstract also has a copy of the rest of the paper. You cannot refer to figures or data that are presented in the body of the paper. Since abstracts are used in literature searches, all key words that describe the paper should be included in the abstract. Be quantitative with results and keep it to less than 100 words.

### Introduction

This section outlines the background necessary to introduce your results. It is not an abbreviated review of what you are going to discuss in detail later. This section should present the necessary theoretical and experimental context such that a knowledgeable colleague, who is not an expert in the field, will be able to understand the data presentation and discussion. If you are going to use a particular theoretical model to extract some information from your data, this model should be discussed in the introduction.

Where appropriate, factual information should be referenced. When presenting background information, you may guide the reader to a detailed description of a particular item with a statement such as: "A more detailed discussion of laminar flow can be found elsewhere.<sup>1</sup>" If you know where there is a good discussion of some item, you should not repeat it.

How one proceeds from this point depends upon whether the paper is about a theoretical study or an experiment. We will first suggest a format for papers about experimental investigations and then one that describes a theoretical derivation.

## Experimental Investigations

### *The Experiment*

This section guides the reader through the techniques and apparatus used to generate the data. Schematic diagrams of equipment and circuits are often easier to understand than prose descriptions. A statement such as "A diagram of the circuit used to measure the stopping potential is shown in Fig. 6" is better than a long set of words. It is not necessary to describe in words what is shown in a diagram unless the average reader would not be able to follow the diagram. If special experimental techniques were developed as part of this work, they should be discussed here. You should separate the discussion of the equipment used to measure something from your results. This section should not include data presentations or discussions of error analysis.

### *Data Presentation and Interpretation of Results*

The data are the truths of your work. This section should lead the reader through the data and how errors were measured or assigned. The numerical data values should be presented in tables and figures, each with its own number and caption, e.g., "The results of the conductivity measurements are shown in Table 3." It is difficult to follow narratives when the numerical results are included as part of the narrative. Raw, unanalyzed data should not be presented in the paper. All figures and tables should be referred to by their number. Any figure or table that is not discussed in the narrative should be eliminated. Items which are not discussed have no place in a paper.

## Theoretical Studies

### *The Model*

This part should consist of a theoretical development of the constructs used to model the physical system under investigation. Equations should be on separate lines and numbered consecutively. The letters or symbols used in the equations should be identified in the narrative, e.g., "The potential can be approximated as:

$$W \approx Z - \sigma(\rho) \quad (1)$$

where  $Z$  is the number of protons and  $\sigma$  is the screening constant that is dependent on the charge density,  $\rho$ , of the inner electrons of the  $K$  and  $L$  shells." If you wish to use this equation at a later time in the narrative, refer to it by its number, e.g., "The straight line fit shown in Fig. 3 indicates that Eq. (1) can be used to extract a value of..."

### *Calculations*

This section presents a summary and discussion of the numerical results calculated from the model. The results should be presented in tables or graphs, each with a caption. A table or graph that is not discussed in the narrative should be eliminated. Data that are not interpreted by the writer have no place in a paper. Reference numerical results that are used in the calculations and come from previous work done by others.

## Conclusion

In this section, briefly summarize the key result and supporting argument. Be sure to list important quantities and, if appropriate, where this research could lead in the future.

## References

All references, numbered in order of appearance, are collected together at the end of the paper. Note that in most cases you do not need to include article titles. Additional formatting guidance for JURP submissions is available on the JURP website and AIP Publishing's website. See the references for examples.<sup>1-6</sup>

## Other Advice

### *Tables and Figures*

Readers often scan papers by looking at the figures and data tables before they read the narrative of the work. Each table or figure should be numbered and have a descriptive caption. Take care to put enough information in the caption that the reader can get some feeling for the meaning of the data presentation. In some journals, tables and figures are placed by the layout editors at the corners of the page to make the format attractive and easy to read, so a figure may not even be on the same page as the discussion of that figure. All lines shown on graphs should be identified, e.g., "The dashed line is drawn to guide the eye" or "The solid line is a fit to the data using the Ising model."

An example of a graph of a set of data is shown in Figure 1. The graph is sized by the range of data points. The bottom left point does not have to be the origin (0, 0). Error bars must be shown with data points. A graph with all the data points clustered in one small corner and lots of white space does not help the reader get a feeling of the dependence of your data. Be careful that the figures you present are not too busy; too much information on a figure makes it difficult to pick out the important parts. Remember that figures often appear much smaller in print so make sure graph fonts are about the same size as in the narrative. Also, color plots could be more expensive to print than black and white and not convey the information any more clearly. Black filled vs empty symbols or solid vs dashed lines offer high contrast on a plot that will be reduced in size for publication. Figures should have high resolution or they may appear blurry.

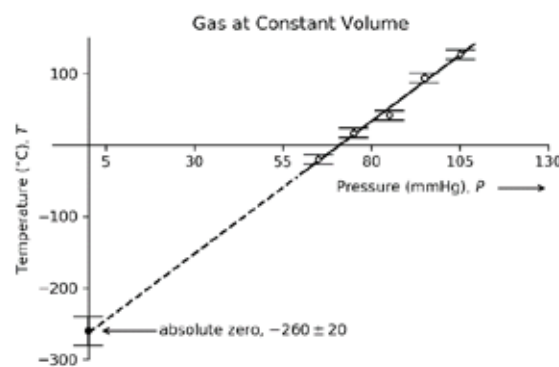


**FIGURE 1.** A graph of gas temperature versus pressure for an ideal gas at constant volume. The solid line drawn is the least squares fit straight line to the data. The dashed line extrapolates to the intercept, with uncertainty, denoting an estimate of absolute zero. This figure is adapted from John Taylor's *An Introduction to Error Analysis* 2nd Edition. The figure should be centered. To help stay within the space requirement consider having two figures next to each other. If figures have more than one part, each part should be labeled (a), (b), etc.

**TABLE 1.** Energy states found in the numerical search. The accepted values for these states are also listed.

State	Experimental $eV$	Theoretical $eV$
3S	$5.15 \pm 0.01$	5.13
4S	$1.89 \pm 0.02$	1.93
3P	$2.96 \pm 0.01$	3.02

### Numbers and Units

Any experimentally measured data presented in tables, such as that shown in Table 1, should include uncertainties. You should use scientific notation when presenting numbers,  $(7.34 \pm 0.03) \times 10^7$  eV. Take care that you have the correct number of significant digits in your results; just because the device shows six digits, does not mean that they are significant. You should use the MKS system of units.

### Style

It is often helpful to make an outline of your paper, with figures, before you write it. In this way, you can be sure that the logical development of your presentation does not resemble two octopuses fighting, but that it is linear. Often the order of your journal notebook is not the same order in which you should present the data.

One generally writes the report in the past tense. You also should use the third person. Even though you might have done the work by yourself, use "we," e.g., "*We calculated the transition probability for...*" It is often confusing when you begin sentences with conjunctions. Make sure that each sentence is a clear positive statement rather than an apology.

There are a few words or phrases you should be careful of using. **Fact** – This is a legal word and is generally avoided in the physics literature. **Proof or prove** – These words are meaningful in mathematics and you cannot prove something in physics, especially experimental physics. **The purpose of this experiment is** – Through background information we outline the issue we aim to solve. **One can easily show that** – Do not intimidate the reader. Remember that the reader of your paper is a senior in college! **It is obvious that** or **One clearly can see** – Such statements only intimidate the reader that does not find your work trivial. **Data** is the plural form of the noun datum, so use it as such: "The data are" or "The data show that." **Human error** has no specific meaning but instead indicates an unspecified error. Errors must be quantified, not swept under a rug and remain unnamed. **In order to** – This phrase can usually be replaced with just the word to. **Almost exactly** – We do not know how can something be almost and exact at the same time.

Adhere strictly to the template and format guidelines required by the publisher of the journal. The newest JGRP templates and formatting guidelines are available online.

Lastly, the journal may request that you suggest reviewers of your manuscript. Reviewers should be as unbiased as possible and knowledgeable of the area of physics you are doing. Possible reviewers are scientists that have recently published in the same or related areas of physics as your manuscript. Good reviewers will offer helpful criticism of your work to improve the manuscript. The journal editor may also offer suggestions to improve the manuscript and ultimately has the responsibility to accept or reject your manuscript or revisions for publication.

### ACKNOWLEDGMENTS

This short section should acknowledge help received from others if it is not referenced in the previous sections. This is where you give credit to a colleague or someone in the machine shop who helped you build a piece of equipment. You may also include your funding source, if appropriate.

### REFERENCES

References should be numbered using Arabic numerals followed by a period (.) as shown below and should follow the format in the examples. Ref. 1 is for a book. Ref. 2 is for a journal article.

1. M. P. Brown and K. Austin, *The New Physique* (Publisher Name, Publisher City, 2005), pp. 25–30.
2. M. P. Brown and K. Austin, *Appl. Phys. Letters* **85**, 2503–2504 (2004).
3. R. T. Wang, "Title of Chapter," in *Classic Physiques*, edited by R. B. Hamil (Publisher Name, Publisher City, 1999), pp. 212–213.
4. C. D. Smith and E. F. Jones, "Load-cycling in cubic press," in *Shock Compression of Condensed Matter-2001*, AIP Conference Proceedings 620, edited by M. D. Furnish *et al.* (AIP Publishing, Melville, NY, 2002), pp. 651–654.
5. B. R. Jackson and T. Pitman, U.S. Patent No. 6,345,224 (8 July 2004).
6. D. L. Davids, "Recovery effects in binary aluminum alloys," Ph.D. thesis, Harvard University, 1998.
7. R. C. Mikkelsen (private communication).

## Supporting Physics and Astronomy Join SPS Today!

With an SPS membership, you will gain access to our awards system to apply for scholarships, internships, research grants, and much more!

An SPS Membership Gives You:

- A monthly copy of *Physics Today*
- A quarterly copy of the *SPS Observer*
- Access to our awards system to apply for scholarships, internships, and research grants
- **FREE** membership to two of AIP's member societies for up to 3 years
- **FREE** joint membership to the National Society of Black Physicists (NSBP) or the National Society of Hispanic Physicists (NSHP)
- And More!

Individual membership is only \$24.00 per year. Discounts are available for group and chapter memberships! Learn more here: [www.spsnational.org/about/membership](http://www.spsnational.org/about/membership)

 JURPJOURNAL *of*  
UNDERGRADUATE  
REPORTS IN PHYSICS

## What is JURP?

The Journal of Undergraduate Reports in Physics (JURP) is a peer-reviewed publication of the society of Physics Students comprised of research, outreach, and scholarly reporting.

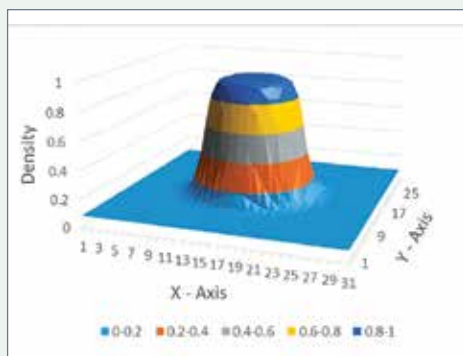
JURP provides exposure for SPS members conducting physics research while also supporting faculty who conduct undergraduate research and scholarship through peer-reviewed publication.

### Research

Peer-reviewed papers within any area of physics research  
Accepted research submissions will be indexed and searchable

### Scholarship

Independent research across all of physical sciences: physics, quantum, astronomy, engineering physics, astrophysics, optics, mathematical physics, nano-science, acoustics, meteorology, physics education, particle physics, electronics, medical physics, and more



## Submit Your Report!

All current SPS members are eligible to submit to JURP. The author(s) must have performed all the work reported in the paper as an undergraduate student.

SPS National will accept submissions to JURP on a rolling basis, but the final deadline for the print edition is **March 15**.